

Nonlinear burn control in ITER using adaptive allocation of actuators with uncertain dynamics

V. Graber*  and E. Schuster

Lehigh University, Bethlehem, PA 18015-3085, United States of America

E-mail: graber@lehigh.edu

Received 29 May 2021, revised 26 October 2021

Accepted for publication 24 November 2021

Published 22 March 2022




CrossMark

Abstract

ITER will be the first tokamak to sustain a fusion-producing, or burning, plasma. If the plasma temperature were to inadvertently rise in this burning regime, the positive correlation between temperature and the fusion reaction rate would establish a destabilizing positive feedback loop. Careful regulation of the plasma's temperature and density, or burn control, is required to prevent these potentially reactor-damaging thermal excursions, neutralize disturbances and improve performance. In this work, a Lyapunov-based burn controller is designed using a full zero-dimensional nonlinear model. An adaptive estimator manages destabilizing uncertainties in the plasma confinement properties and the particle recycling conditions (caused by plasma-wall interactions). The controller regulates the plasma density with requests for deuterium and tritium particle injections. In ITER-like plasmas, the fusion-born alpha particles will primarily heat the plasma electrons, resulting in different electron and ion temperatures in the core. By considering separate response models for the electron and ion energies, the proposed controller can independently regulate the electron and ion temperatures by requesting that different amounts of auxiliary power be delivered to the electrons and ions. These two commands for a specific control effort (electron and ion heating) are sent to an actuator allocation module that optimally maps them to the heating actuators available to ITER: an electron cyclotron heating system (20 MW), an ion cyclotron heating system (20 MW), and two neutral beam injectors (16.5 MW each). Two different actuator allocators are presented in this work. The first actuator allocator finds the optimal mapping by solving a convex quadratic program that includes actuator saturation and rate limits. It is nonadaptive and assumes that the mapping between the commanded control efforts and the allocated actuators (i.e. the effector model) contains no uncertainties. The second actuator allocation module has an adaptive estimator to handle uncertainties in the effector model. This uncertainty includes actuator efficiencies, the fractions of neutral beam heating that are deposited into the plasma electrons and ions, and the tritium concentration of the fueling pellets. Furthermore, the adaptive allocator considers actuator dynamics (actuation lag) that contain uncertainty. This adaptive allocation algorithm is more computationally efficient than the aforementioned nonadaptive allocator because it is computed using dynamic update laws so that finding the solution to a static optimization problem is not required at every time step. A simulation study assesses the performance of the proposed adaptive burn controller augmented with each of the actuator allocation modules.

Keywords: burn control, ITER, actuator dynamics, adaptive estimation, control allocation

* Author to whom any correspondence should be addressed.

 Supplementary material for this article is available [online](#)

(Some figures may appear in colour only in the online journal)

1. Introduction

The regulation of temperature and density in a fusion-producing (burning) plasma in ITER will require the use of nonlinear burn control algorithms [1–4] that request the correct amounts of external heating and fueling for equilibrium stabilization [5]. Because the fast ions introduced from neutral beam injection (NBI) and fusion reactions, as well as the heating by other auxiliary sources, unevenly heat the plasma ion and electron populations [6, 7], the ion and electron temperatures will not be necessarily coupled. In previous work [8], the authors used Lyapunov techniques [5] to design a nonlinear burn controller based on a two-temperature plasma model. This model assumed that the ion and electron temperatures were proportional through an uncertain parameter, and the burn controller regulated both temperatures with one control law for the total auxiliary heating. Complex phenomena, such as the aforementioned ion–electron temperature relationship, were modeled with some level of uncertainty. Throughout this work, uncertainty in the model is given by specific parameters that are not precisely known to the control scheme. This uncertainty can degrade the control performance. The adaptive estimation scheme presented in [8] was designed to counter this hurdle. This prior work [8] was extended in [9] by basing the controller on a two-temperature model with separate response models for the ion and electron energies. In contrast to [8], this burn controller used two unique stabilizing control laws for the external ion and electron heating. In both [8, 9], control laws for the external deuterium and tritium injection rates were used to regulate the plasma density.

ITER's controllers will have access to a diverse suite of actuators that can be used to generate the external heating and fueling necessary for the regulation of the burn condition. Two pellet injectors will be the primary source of external fueling in ITER. One injector supplies pure deuterium (D) pellets, and the other injector supplies a mixture of deuterium and tritium (T). The tritium concentration in the mixed DT pellets will be nominally 90%, but it can vary during plasma operations [10]. An ion cyclotron (IC) heating system, an electron cyclotron (EC) heating system, and two neutral beam injectors (NBI) will be used for plasma heating in ITER [11]. With six actuators (D pellet injector, DT pellet injector, IC, EC, NBI #1 and NBI #2) and four virtual control efforts requested by the controller (D fueling, T fueling, ion heating and electron heating), an actuator allocation algorithm can be used to optimally map the virtual control efforts to the available actuators. The mapping between the virtual control efforts and the efforts produced by the actuators (i.e. actuation efforts) is known as the effector model [12].

The actuators available to a tokamak must be properly managed to meet the different and sometimes competing

controller's requests for external heating and fueling. Actuator management of auxiliary heating systems has been experimentally tested for electron temperature control [13]. The manager checks each actuator for operational readiness and availability (e.g. electron cyclotron heating is temporarily disabled for diagnostic purposes after a pellet injection event) among other conditions. In [14], individual controllers for internal inductance and normalized beta regulation are integrated using an actuator manager. This actuator manager attempts to achieve different control objectives simultaneously using real-time optimization. Furthermore, a larger number of individual controllers were integrated under an optimization-based actuator manager and tested experimentally on DIII-D [15].

There are advantages to handling the actuators with an actuator allocator instead of including them directly in the design of the burn controller. Because the actuator allocator is designed separately from the burn controller, reconfigurations in the set of actuators available for burn control do not require modification of the virtual control laws [16]. This modularity allows the actuator allocator to be swapped for another without changing controllers. As an example, a scenario could occur where only one NBI is available for burn control in ITER. The other NBI may be needed for objectives outside the scope of burn control. Without changing the controller, ITER operators could exchange an actuator allocator that considers two neutral beam injectors with a different one that considers only one neutral beam injector.

In this work, the proposed model-based burn controller and actuator allocator improve upon those presented in prior work [9] in numerous aspects. First, the actuator allocation algorithm in this work is more computationally efficient. The actuator allocator in [9] mapped the virtual control efforts for the ion and electron heating to the IC, EC and NBI systems by solving a quadratic program at every time step. This is slower than the dynamic update laws [17] that the actuator allocator in this work uses for the mapping. Second, unlike the prior work [9], the actuator allocator in this work considers the plasma fueling and pellet injectors. Third, uncertainty is introduced into the effector model by assuming that various parameters in it are uncertain. The uncertain constants in the effector model include the actuator efficiency factors, the neutral beam heating fractions for the ions and electrons, and the tritium fraction of the DT fueling pellets. This uncertainty is handled by including an adaptive estimation scheme within the actuator allocator. In [9], the nonadaptive allocator was based on an effector model that did not include any uncertainty. Fourth, this work introduces actuator dynamics in the form of actuation lag. Actuation lag results from various sources such as the thermalization delay of neutral beam particles and the flight time of pellets traveling through their guide tubes which lead into the plasma. The effects of the actuators

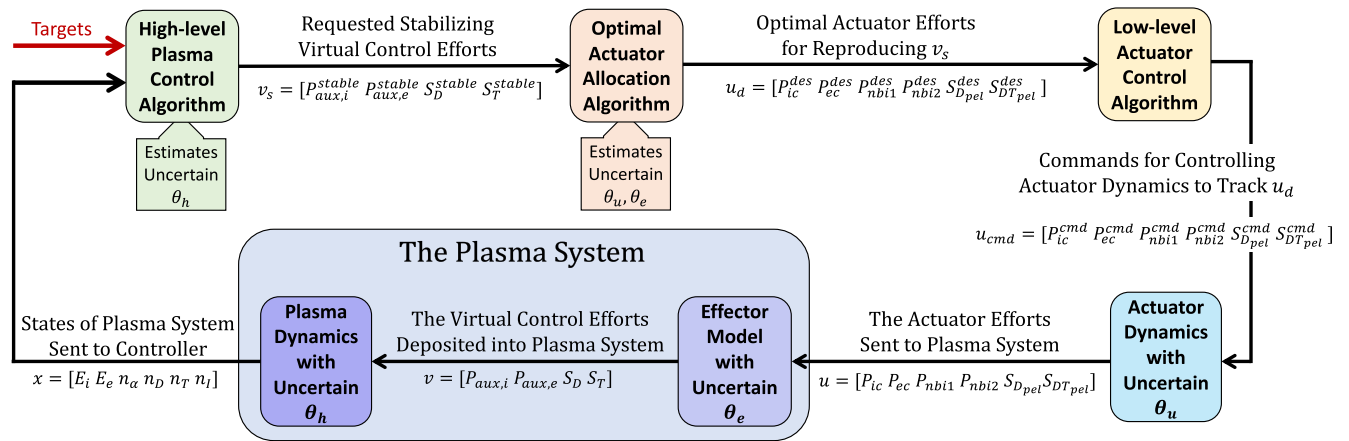


Figure 1. This flow chart represents the closed-loop system with the plasma system, a burn controller, an actuator allocation algorithm and actuator dynamics. For the simulations presented in section 10, the block labeled ‘the plasma system’ (which contains the plasma dynamics and the effector model) and the block for the actuator dynamics (the bottom row of blocks) represent the plant. The remaining blocks (the top row) represent the burn control scheme that attempts to regulate the plant.

on the plasma were assumed to be instantaneous in prior work [8, 9]. In this work, the actuation lag is considered to be uncertain, and yet another adaptive estimator is employed to handle this additional uncertainty. Finally, the burn controller that provides requested virtual control efforts to the allocator was modified to consider more uncertainty in the plasma model. The proposed adaptive burn controller estimates the uncertain plasma confinement conditions, the DT recycling and impurity sputtering from plasma–wall interactions [18], and the alpha-particle heating fractions for the ions and electrons.

Using the aforementioned modularity of the actuator allocation algorithms, this work presents two burn control schemes. The first one is the new adaptive burn controller (with the expanded adaptive estimation scheme) augmented with the nonadaptive, static allocator from [9]. The second one is the new adaptive burn controller augmented with the new adaptive, dynamic allocator (that considers actuator dynamics). A nonlinear simulation study evaluates the performance of both of these burn control schemes.

This paper is organized as follows. Section 2 provides a high-level description of the closed-loop plasma system. In section 3, the plasma model is presented. Control objectives are considered in section 4. The stabilizing controller is synthesized in section 5. In section 6, the effector model is discussed. Actuator dynamics are covered in section 7. The nonadaptive, static actuator allocator is presented in section 8. In section 9, the adaptive, dynamic allocator is proposed. The simulation study in section 10 evaluates the burn control performance of the adaptive controller augmented with both allocators. Conclusions and future work are addressed in section 11.

2. Description of the closed-loop system

Figure 1 provides a graphical description of the closed-loop plasma system with actuator allocation and actuator dynamics. The burning plasma dynamics consists of six (measured) states: the ion energy E_i , the electron energy E_e , the alpha-particle density n_α , the deuterium density n_D , the tritium

density n_T , and the impurity density n_I . Uncertain parameters such as the alpha-particle ion-heating fraction, the deuterium–tritium wall recycling, the impurity sputtering and the plasma confinement quality are lumped into θ_h . The high-level burn controller determines the virtual control efforts that will stabilize the target equilibrium of the nonlinear plasma system. The four virtual control efforts are the auxiliary ion heating $P_{aux,i}$, the auxiliary electron heating $P_{aux,e}$, the deuterium fueling S_D , and the tritium fueling S_T . Adaptive laws provide estimate θ_h to handle uncertainty in the plasma conditions.

The actuator allocator receives the requested stabilizing virtual control efforts v_s from the high-level burn controller. Using either a static optimization problem or dynamic update laws, it determines the optimal actuation efforts u_d for reproducing v_s . The low-level actuator controller receives the optimal actuation efforts u_d from the allocator, and it determines what commands u_{cmd} should be sent to the actuators in order to track u_d despite the actuator dynamics. The actuator dynamics include lags in the actuation and uncertain parameters lumped into θ_u . The six actuation efforts u are the heating from the ion cyclotron actuator P_{ic} , the heating from the electron cyclotron actuator P_{ec} , the heating from the two neutral beam injection actuators P_{nbi1} and P_{nbi2} , the fueling from the deuterium pellet injection actuator $S_{D,pel}$, and the fueling from the deuterium–tritium pellet injection actuator $S_{DT,pel}$. After experiencing lag, the actuation efforts u are deposited into the plasma system. As determined by the effector model, the actuation efforts u produce the virtual control efforts v . The effector model contains uncertainty (θ_e) in the actuator efficiencies, the neutral beam ion-heating fraction, and the tritium concentration of the pellets. The adaptive allocator generates estimates θ_e and $\hat{\theta}_u$ to handle the uncertainty. The goal of the allocator is to minimize $|v - v_s|$.

3. The two-temperature plasma model

The presented volume-average model considers that the plasma ions and electrons have unique temperatures, T_i and

T_e , respectively. As a result, the ion and electron energies, E_i and E_e , are governed by separate response models,

$$\dot{E}_i = -\frac{E_i}{\tau_{E,i}} + \phi_\alpha P_\alpha + P_{ei} + P_{aux,i}, \quad (1)$$

$$\dot{E}_e = -\frac{E_e}{\tau_{E,e}} + (1 - \phi_\alpha)P_\alpha - P_{ei} - P_{br} + P_{oh} + P_{aux,e}, \quad (2)$$

where P_α , P_{br} , P_{oh} and P_{ei} are the alpha particle power from fusion, the bremsstrahlung radiation losses, the ohmic heating and the collisional power exchange between the ions and electrons. The fraction of P_α deposited into the plasma ions is ϕ_α . Energy transport out of the plasma is modeled with confinement times $\tau_{E,i}$ and $\tau_{E,e}$. The controlled external heating deposited into the ions and electrons are $P_{aux,i}$ and $P_{aux,e}$. The units of each term are $W m^{-3}$.

The ion and electron energies are related to particle densities such that

$$E = E_i + E_e = \frac{3}{2}(n_D + n_T + n_\alpha + n_i)T_i + \frac{3}{2}n_e T_e, \quad (3)$$

where n_D , n_T , n_α and n_i are the deuterium, tritium, alpha particle and impurity densities. The assumption of quasi-neutrality demands an equal number of protons and electrons in the plasma. Therefore, the electron density is $n_e = n_D + n_T + 2n_\alpha + Z_1 n_i$ where Z_1 is the average impurity atomic number. The density response models are

$$\dot{n}_D = -\frac{n_D}{\tau_D} - S_\alpha + S_D + S_D^R, \quad (4)$$

$$\dot{n}_T = -\frac{n_T}{\tau_T} - S_\alpha + S_T + S_T^R, \quad (5)$$

$$\dot{n}_\alpha = -\frac{n_\alpha}{\tau_\alpha} + S_\alpha, \quad (6)$$

$$\dot{n}_i = -\frac{n_i}{\tau_i} + S_i^{sp}. \quad (7)$$

Each term is expressed in units of $m^{-3} s^{-1}$. The particle confinement times are τ_α , τ_D , τ_T and τ_i . Deuterium and tritium particles can be injected into the plasma at the controlled rates of S_D and S_T , respectively. The impurity sputtering source due to plasma-wall interactions is given by $S_i^{sp} = f_i^{sp}(n/\tau_i + \dot{n})$, where f_i^{sp} is the sputtering fraction and $n = n_D + n_T + n_\alpha + n_i + n_e$ is the total plasma density. The wall recycling sources for D and T particle, respectively, are modeled with

$$S_D^R = \frac{1}{1 - f_{ref}(1 - f_{eff})} \left\{ f_{ref} \frac{n_D}{\tau_D} + \left(\frac{n_D}{\tau_D} + \frac{n_T}{\tau_T} \right) \times (1 - \gamma^{PFC}) \left[\frac{(1 - f_{ref}(1 - f_{eff}))R^{eff}}{1 - R^{eff}(1 - f_{eff})} - f_{ref} \right] \right\}, \quad (8)$$

$$S_T^R = \frac{1}{1 - f_{ref}(1 - f_{eff})} \left\{ f_{ref} \frac{n_T}{\tau_T} + \left(\frac{n_D}{\tau_D} + \frac{n_T}{\tau_T} \right) \times \gamma^{PFC} \left[\frac{(1 - f_{ref}(1 - f_{eff}))R^{eff}}{1 - R^{eff}(1 - f_{eff})} - f_{ref} \right] \right\}, \quad (9)$$

where f_{eff} is the fueling efficiency of recycled particles, f_{ref} is the fraction of escaping particles reflected back into the plasma, R^{eff} is the global recycling coefficient, and γ^{PFC} is the tritium fraction of the recycled particles [18].

The DT fusion reaction rate density is given by $S_\alpha = n_D n_T \langle \sigma v \rangle$ where the DT reactivity, $\langle \sigma v \rangle$, is

$$\langle \sigma v \rangle = C_1 \omega \sqrt{\xi / (m_r c^2 T_i^3)} e^{-3\xi}, \quad \xi = (B_G^2 / 4\omega)^{1/3},$$

$$\omega = T_i \left[1 - \frac{T_i(C_2 + T_i(C_4 + T_i C_6))}{1 + T_i(C_3 + T_i(C_5 + T_i C_7))} \right]^{-1}, \quad (10)$$

where T_i is expressed in keV and B_G , $m_r c^2$ and C_j for $j \in \{1, \dots, 7\}$ are constants [19]. Because every reaction creates an alpha particle with $Q_\alpha = 3.52$ MeV of kinetic energy, the alpha particle power is $P_\alpha = Q_\alpha S_\alpha$. In contrast to the DT reactivity, the bremsstrahlung radiation losses and the ohmic heating are determined by the electron temperature. They are given by

$$P_{br} = 5.5 \times 10^{-37} Z_{eff}^2 n_e^2 \sqrt{T_e}, \quad (11)$$

$$P_{oh} = 2.8 \times 10^{-9} Z_{eff}^2 I_p^2 a^{-4} T_e^{-3/2}, \quad (12)$$

where $Z_{eff} = (n_D + n_T + 4n_\alpha + Z_1^2 n_i) / n_e$ is the effective atomic number, I_p is the plasma current, and a is the plasma minor radius. The power that is exchanged between the plasma ions and electrons through collisions is given by

$$P_{ei} = \frac{3}{2} n_e \frac{T_e - T_i}{\tau_{ei}}, \quad \tau_{ei} = \frac{3\pi\sqrt{2}\pi\epsilon_0^2 T_e^{3/2}}{e^4 m_e^{1/2} \ln \Lambda_{ei}} \sum_{ions} \frac{m_i}{n_i Z_i^2}, \quad (13)$$

where τ_{ei} is the relaxation time [20], the electron mass is $m_e = 9.1096 \times 10^{-31}$ kg, $e = 1.622 \times 10^{-19}$ C, $\epsilon_0 = 8.854 \times 10^{-12}$ F m^{-1} , T_e has units of J, and the natural logarithm is $\Lambda_k = 1.24 \times 10^7 T_k^{3/2} / (n_e^{1/2} Z_{eff}^2)$ for $k \in \{i, e\}$.

The global energy confinement time is determined from the IPB98(y, 2) scaling law [21]. The scaling law is

$$\tau_E = H \tau_E^{sc} = H_H \times 0.0562 I_p^{0.93} B_T^{0.15} M^{0.19} \times R^{1.97} \epsilon^{0.58} \kappa^{0.78} P^{-0.69} V^{-0.69} n_{e19}^{0.41}, \quad (14)$$

where H_H is the H -factor which depends on quality of the plasma confinement, R is the plasma major radius, B_T is the toroidal magnetic field, $\epsilon = a/R$, κ is the vertical elongation at 95% flux surface, V is the volume of the plasma, n_{e19} is n_e in $10^{19} m^{-3}$, and $M = 3\gamma + 2(1 - \gamma)$ [22]. The tritium fraction, γ , is equal to the ratio n_T / n_H where $n_H = n_D + n_T$. The total plasma power, $P = P_{aux,i} + P_{aux,e} - P_{br} + P_\alpha + P_{oh}$, is expressed in $MW m^{-3}$. The machine parameters I_p , B_T , R , a , κ and V , respectively, have values of 15 MA, 5.3 T, 6.2 m, 2 m, 1.7 and 837 m^3 for ITER [22]. With uncoupled temperatures, ions and electrons have different energy transport rates. Therefore, $\tau_{E,i} = \zeta_i \tau_E$ and $\tau_{E,e} = \zeta_e \tau_E$ where ζ_i and ζ_e are constants. Particle confinement times are similarly proportional to (14) such that $\tau_r = k_r \tau_E$ for $r \in \{\alpha, D, T, I\}$.

Fusion reactions and NBI heat the plasma through the introduction of fast ions. Initially, these fast ions primarily heat

electrons. As their kinetic energy falls due to collisional events, increasingly more of their energy goes into the plasma ions. Only at the critical energy, ε_c , do the fast ions evenly heat the plasma ions and electrons. The ion heating fraction is denoted as ϕ_f for $f \in \{\alpha, \text{nbi}\}$ to distinguish between alpha-particle heating and neutral beam heating. In prior work [9], the ion heating fraction was shown to be

$$\phi_f = \frac{1}{x_0} \left[\frac{1}{3} \ln \frac{1-x_0^{\frac{1}{2}}+x_0}{(1+x_0^{\frac{1}{2}})^2} + \frac{2}{\sqrt{3}} \left(\tan^{-1} \frac{2x_0^{\frac{1}{2}}-1}{\sqrt{3}} + \frac{\pi}{6} \right) \right], \quad (15)$$

$$\varepsilon_c = \frac{A_f T_e}{m_e^{1/3} n_e^{2/3}} \sum_{\text{ions}} n_i Z_i^2 \left(\frac{3\sqrt{\pi} \ln \Lambda_i}{4 \ln \Lambda_e} \right)^{\frac{2}{3}},$$

where $x_0 = \varepsilon_{f0}/\varepsilon_c$, ε_{f0} is the initial kinetic energy of the fast ion, A_f for $f \in \{\alpha, \text{nbi}\}$ is the atomic mass of the fast ion, and A_i for $i \in \{\alpha, \text{D}, \text{T}, \text{I}\}$ is the atomic mass of the plasma ions [6, 23]. For the alpha particles produced from fusion events, $\varepsilon_{\alpha 0} = Q_\alpha$ and $A_\alpha = 4$. ITER's neutral beam heating system injects 1 MeV deuterium particles into the plasma [24]. Therefore, $\varepsilon_{\text{nbi}0} = 1$ MeV and $A_{\text{nbi}} = 2$. For the plasma temperatures and densities considered in this paper's simulation study of ITER (section 10), $\phi_\alpha \approx 15\%$ and $\phi_{\text{nbi}} \approx 20\%$.

The following parameters are considered to be uncertain: H_H , ζ_i , ζ_e , ϕ_α , k_D , k_T , k_α , k_I , f_{eff} , f_{ref} , R^{eff} , γ^{PFC} and f_1^{SP} . They are lumped into the nominal uncertainty vector θ_h such that (1), (2) and (4) through (7) can be rewritten as

$$\begin{aligned} \dot{E}_i &= -\theta_{h,1} \frac{E_i}{\tau_E^{\text{sc}}} + \theta_{h,3} P_\alpha + P_{\text{ei}} + P_{\text{aux},i}, \\ \dot{E}_e &= -\theta_{h,2} \frac{E_e}{\tau_E^{\text{sc}}} + \theta_{h,4} P_\alpha - P_{\text{ei}} - P_{\text{br}} + P_{\text{oh}} + P_{\text{aux},e}, \\ \dot{n}_\alpha &= -\theta_{h,5} \frac{n_\alpha}{\tau_E^{\text{sc}}} + S_\alpha, \\ \dot{n}_D &= -\theta_{h,6} \frac{n_D}{\tau_E^{\text{sc}}} + \theta_{h,9} \frac{n_T}{\tau_E^{\text{sc}}} - S_\alpha + S_D, \\ \dot{n}_T &= -\theta_{h,7} \frac{n_T}{\tau_E^{\text{sc}}} + \theta_{h,10} \frac{n_D}{\tau_E^{\text{sc}}} - S_\alpha + S_T, \\ \dot{n}_I &= -\theta_{h,8} \frac{n_I}{\tau_E^{\text{sc}}} + \theta_{h,11} \frac{n}{\tau_E^{\text{sc}}} + \theta_{h,12} \dot{n}, \end{aligned} \quad (16)$$

where $\theta_{h,i}$ is the i th element of θ_h . The elements of θ_h are given in appendix A, and they can be inferred from (1), (2), (4)–(9) and (16).

4. Burn control objectives

The purpose of the high-level controller is to track equilibria defined by (16) at steady-state despite the uncertainty in θ_h . The desired equilibrium values for the six states (\bar{E}_i , \bar{E}_e , \bar{n}_α , \bar{n}_D , \bar{n}_T , \bar{n}_I) and the four virtual control efforts ($\bar{P}_{\text{aux},i}$, $\bar{P}_{\text{aux},e}$, \bar{S}_D , \bar{S}_T) are determined by solving the system of six equation (16) at steady-state with predefined values for \bar{E}_i , \bar{E}_e , \bar{n} and $\bar{\gamma}$.

These equations can be used to study ITER's operational space, which in turn is usually represented by Plasma Operation Contour (POPCON) diagrams [25]. The deviations of the states from desired values are denoted as $\tilde{E}_i = E_i - \bar{E}_i$, $\tilde{E}_e = E_e - \bar{E}_e$, $\tilde{n}_\alpha = n_\alpha - \bar{n}_\alpha$, $\tilde{n}_D = n_D - \bar{n}_D$, $\tilde{n}_T = n_T - \bar{n}_T$ and $\tilde{n}_I = n_I - \bar{n}_I$. The control objective is to drive the following system to its equilibrium at the origin (i.e. drive the deviations to zero) despite model uncertainties:

$$\begin{aligned} \dot{\tilde{E}}_i &= -\theta_{h,1} \frac{\tilde{E}_i + \bar{E}_i}{\tau_E^{\text{sc}}} + \theta_{h,3} P_\alpha + P_{\text{ei}} + P_{\text{aux},i}, \\ \dot{\tilde{E}}_e &= -\theta_{h,2} \frac{\tilde{E}_e + \bar{E}_e}{\tau_E^{\text{sc}}} + \theta_{h,4} P_\alpha - P_{\text{ei}} - P_{\text{br}} + P_{\text{oh}} + P_{\text{aux},e}, \\ \dot{\tilde{n}}_\alpha &= -\theta_{h,5} \frac{\tilde{n}_\alpha + \bar{n}_\alpha}{\tau_E^{\text{sc}}} + S_\alpha, \\ \dot{\tilde{n}}_D &= -\theta_{h,6} \frac{\tilde{n}_D + \bar{n}_D}{\tau_E^{\text{sc}}} + \theta_{h,9} \frac{\tilde{n}_T + \bar{n}_T}{\tau_E^{\text{sc}}} - S_\alpha + S_D, \\ \dot{\tilde{n}}_T &= -\theta_{h,7} \frac{\tilde{n}_T + \bar{n}_T}{\tau_E^{\text{sc}}} + \theta_{h,10} \frac{\tilde{n}_D + \bar{n}_D}{\tau_E^{\text{sc}}} - S_\alpha + S_T, \\ \dot{\tilde{n}}_I &= -\theta_{h,8} \frac{\tilde{n}_I + \bar{n}_I}{\tau_E^{\text{sc}}} + \theta_{h,11} \frac{\tilde{n} + \bar{n}}{\tau_E^{\text{sc}}} + \theta_{h,12} \dot{\tilde{n}}. \end{aligned} \quad (17)$$

Appendix B provides the dynamic equations for $\tilde{\gamma}$ and \tilde{n} , which are functions of \tilde{n}_α , \tilde{n}_D , \tilde{n}_T , \tilde{n}_I .

5. Adaptive burn control algorithm

A Lyapunov candidate function $V_z(z)$ [5], where z is the state of the system $\dot{z} = f(z(t))$ with an equilibrium at the origin, can be viewed as a representation of the energy of the dynamic system. If a feedback controller is designed to enforce that the energy is always dissipated ($\dot{V}_z(z) < 0$) except at $z = 0$, then the origin is asymptotically stable and the designed feedback controller is asymptotically stabilizing. Therefore, Lyapunov-based control design follows a two-step procedure: (1) definition of an energy-type Lyapunov candidate function $V_z(z)$; (2) synthesis of control laws that make $\dot{V}_z(z) < 0$ everywhere except at the equilibrium point.

The control laws for the ion heating $P_{\text{aux},i}$, electron heating $P_{\text{aux},e}$, deuterium fueling S_D and tritium fueling S_T are developed using the following Lyapunov function [5]:

$$V = k_i^2 \tilde{E}_i^2 + k_e^2 \tilde{E}_e^2 + k_\gamma^2 \tilde{\gamma}^2 + \tilde{n}^2 + \tilde{\theta}_h^T \Gamma_h^{-1} \tilde{\theta}_h, \quad (18)$$

where k_i , k_e and k_γ are positive constants, and Γ_h is a positive definite matrix. The controller's current estimate of nominal θ_h is $\hat{\theta}_h$ (θ_h is not known). The $\tilde{\theta}_h$ vector is the controller's estimation error of θ_h such that $\tilde{\theta}_h = \hat{\theta}_h - \theta_h$. With the Lyapunov analysis presented in appendix B, the four control laws are formulated as

$$P_{\text{aux},i}^{\text{stable}} = \hat{\theta}_{h,1} \frac{\tilde{E}_i}{\tau_E^{\text{sc}}} - \hat{\theta}_{h,3} P_\alpha - P_{\text{ei}}, \quad (19)$$

$$P_{\text{aux},e}^{\text{stable}} = \hat{\theta}_{h,2} \frac{\tilde{E}_e}{\tau_E^{\text{sc}}} - \hat{\theta}_{h,4} P_\alpha + P_{\text{ei}} + P_{\text{br}} - P_{\text{oh}}, \quad (20)$$

$$S_D^{\text{stable}} = \frac{1}{2} \left[3\hat{\theta}_{h,5} \frac{n_\alpha}{\tau_E^{\text{sc}}} + 2\hat{\theta}_{h,7} \frac{n_T}{\tau_E^{\text{sc}}} + 2\hat{\theta}_{h,6} \frac{n_D}{\tau_E^{\text{sc}}} + S_\alpha - 2S_T - (Z_1 + 1) \left(-\hat{\theta}_{h,8} \frac{n_I}{\tau_E^{\text{sc}}} \right) - 2\hat{\theta}_{h,9} \frac{n_T}{\tau_E^{\text{sc}}} - 2\hat{\theta}_{h,10} \frac{n_D}{\tau_E^{\text{sc}}} - (Z_1 + 1)\hat{\theta}_{h,11} \frac{n}{\tau_E^{\text{sc}}} - (Z_1 + 1)\hat{\theta}_{h,12}\dot{n} - K_N\tilde{n} \right], \quad (21)$$

$$S_T^{\text{stable}} = -K_T\tilde{\gamma} + \hat{\theta}_{h,7} \frac{n_T}{\tau_E^{\text{sc}}} + S_\alpha - \hat{\theta}_{h,10} \frac{n_D}{\tau_E^{\text{sc}}} + \gamma \left(\hat{\theta}_{h,5} \frac{3n_\alpha}{2\tau_E^{\text{sc}}} + \frac{(Z_1 + 1)}{2} \left(\hat{\theta}_{h,8} \frac{n_I}{\tau_E^{\text{sc}}} \right) - \frac{3}{2}S_\alpha - \frac{(Z_1 + 1)}{2}\hat{\theta}_{h,11} \frac{n}{\tau_E^{\text{sc}}} - \frac{(Z_1 + 1)}{2}\hat{\theta}_{h,12}\dot{n} - \frac{K_N\tilde{n}}{2} \right), \quad (22)$$

where K_N and K_T are positive constants. The control laws are augmented with an adaptive estimator for the uncertain (not known) θ_h :

$$\dot{\hat{\theta}}_h \approx \dot{\theta}_h = \Gamma_h \begin{bmatrix} -(\bar{E}_i/\tau_E^{\text{sc}})k_i^2\tilde{E}_i \\ -(\bar{E}_e/\tau_E^{\text{sc}})k_e^2\tilde{E}_e \\ P_\alpha k_i^2\tilde{E}_i \\ P_\alpha k_e^2\tilde{E}_e \\ -3\tilde{n}(n_\alpha/\tau_E^{\text{sc}}) \\ -[2\tilde{n} - ((k_\gamma^2\tilde{\gamma})/n_H)](n_D/\tau_E^{\text{sc}}) \\ -[2\tilde{n} - (\gamma - 1)(k_\gamma^2\tilde{\gamma})/n_H](n_T/\tau_E^{\text{sc}}) \\ -\tilde{n}(Z_1 + 1)(n_I/\tau_E^{\text{sc}}) \\ -(((k_\gamma^2\tilde{\gamma})/n_H)\gamma - 2\tilde{n})(n_T/\tau_E^{\text{sc}}) \\ -(\gamma - 1)((k_\gamma^2\tilde{\gamma})/n_H)(n_D/\tau_E^{\text{sc}}) \\ \tilde{n}(Z_1 + 1)(n/\tau_E^{\text{sc}}) \\ (Z_1 + 1)\tilde{n}\dot{n} \end{bmatrix}. \quad (23)$$

Note that $\dot{\hat{\theta}}_h \approx \dot{\theta}_h$ because changes in the uncertain parameters are assumed to be negligible ($\dot{\theta}_h \approx 0$). This assumption implies that these uncertain parameters are either constant or slowly varying when compared with the characteristic time of the system, which is in general the case in practice. The adaptive control laws (19)–(23) track the equilibria of the error system (17) despite the uncertainty in the model. The stability of this adaptive burn controller is discussed in appendix B.

6. Effector model

For the purposes of burn control of the plasma core, ITER will have access to four external heating systems and two external fueling systems. Respectively, the ion cyclotron (IC) and electron cyclotron (EC) systems deliver powers P_{ic} and P_{ec} directly to the ions and electrons. Heat is then transferred between the ion and electron populations through particle collisions. This is

modeled using P_{ei} in (1) and (2). The two neutral beam injection (NBI) systems deliver powers P_{nbi_1} and P_{nbi_2} with ion-heating fraction ϕ_{nbi} and electron-heating fraction $(1 - \phi_{nbi})$. At an injection rate of $S_{DT_{pel}}$, the DT injector fires pellets that have a nominal 90% T concentration. Because this T concentration $\gamma_{DT_{pel}}$ can change during long pulse operations in ITER, a nonlinear burn controller has been designed to handle unknown variations in the deuterium–tritium concentrations of the fueling lines [26]. Similarly, $\gamma_{DT_{pel}}$ is considered to be uncertain in the effector model in this work. However, this change over time is slow enough to fit the assumptions of the actuator allocator design. Indeed, changes of $\gamma_{DT_{pel}}$ over time are considered negligible in the simulation studies presented in section 10. The D injector fuels the plasma at an injection rate of $S_{D_{pel}}$ with pellets that have no tritium ($\gamma_{D_{pel}} = 0$). The actuation efforts $u = [P_{ic}P_{ec}P_{nbi_1}P_{nbi_2}S_{D_{pel}}S_{DT_{pel}}]^T$ are mapped to the virtual control efforts $v = [P_{aux,i}P_{aux,e}S_D S_T]^T = \Phi(u)$ through the effector model:

$$\begin{aligned} P_{aux,i} &= \eta_{ic}P_{ic} + \eta_{nbi_1}\phi_{nbi}P_{nbi_1} + \eta_{nbi_2}\phi_{nbi}P_{nbi_2}, \\ P_{aux,e} &= \eta_{ec}P_{ec} + \eta_{nbi_1}\bar{\phi}_{nbi}P_{nbi_1} + \eta_{nbi_2}\bar{\phi}_{nbi}P_{nbi_2}, \\ S_D &= \eta_{DT_{pel}}(1 - \gamma_{DT_{pel}})S_{DT_{pel}} + \eta_{D_{pel}}S_{D_{pel}}, \\ S_T &= \eta_{DT_{pel}}\gamma_{DT_{pel}}S_{DT_{pel}}, \end{aligned} \quad (24)$$

where η_a for $a \in \{ic, ec, nbi_1, nbi_2, D_{pel}, DT_{pel}\}$ are actuator efficiency factors and $\bar{\phi}_{nbi} = (1 - \phi_{nbi})$. The efficiency factors and ϕ_{nbi} are considered to be constant and uncertain. The virtual control efforts $P_{aux,i}$, $P_{aux,e}$, S_D and S_T that are produced by the actuation efforts in (24) are inputs to the plasma system (16) described in section 3.

In (24), the ion cyclotron heating (P_{ic}) could have been modeled similarly to the neutral beam heating (P_{nbi_1} and P_{nbi_2}), where separate fractions of P_{ic} would be delivered to the plasma ions and electrons as determined by (15). However, in contrast to neutral beam heating where foreign fast ions are externally injected into the plasma, ion cyclotron heating produces fast ions within the plasma by growing a tail in the high-energy region of the ions' distribution function [23]. These native fast ions then heat the surrounding plasma through particle collisions. Therefore, since ion cyclotron heating (P_{ic}) directly impacts the ion energy (E_i) and the resulting change to E_i causes electron heating through particle collisions (which is modeled using P_{ei} in (1) and (2)), the IC heating is chosen to be modeled without explicitly determining ion and electron heating fractions in the effector model (24). Nevertheless, the effector model could be changed to have P_{ic} deliver separate fractions of heating to the ions and electrons as determined by (15) without requiring major changes to the formulation of the actuator allocators presented in sections 8 and 9.

7. Actuator dynamics

Burn control of ITER will have to overcome actuator delays such as the flight time of fueling pellets traveling through guide tubes (the control problem resulting from the pellets' flight time delay has been studied in [27]). The global

plasma response times of the EC, IC, NBI and fueling pellet injection systems could be up to 20 ms, 200 ms, 80 ms and 0.1 s, respectively, for ITER [11]. Therefore, the time between when the actuator command is made by the control scheme and when the actuation efforts u influence the virtual control efforts v through the mapping (24) is nonzero. The instantaneous actuator commands are denoted as $u_{\text{cmd}} = [P_{\text{ic}}^{\text{cmd}} P_{\text{ec}}^{\text{cmd}} P_{\text{nbi}_1}^{\text{cmd}} P_{\text{nbi}_2}^{\text{cmd}} S_{\text{D}_{\text{pel}}}^{\text{cmd}} S_{\text{DT}_{\text{pel}}}^{\text{cmd}}]^T$, and u is the vector of delayed actuation efforts used in (24). The actuator dynamics are modeled as first-order lag processes:

$$T_{\text{lag}} \dot{u} + u = u_{\text{cmd}}, \quad (25)$$

where $T_{\text{lag}} = \text{diag}(\tau_{\text{ic}}^{\text{lag}}, \tau_{\text{ec}}^{\text{lag}}, \tau_{\text{nbi}_1}^{\text{lag}}, \tau_{\text{nbi}_2}^{\text{lag}}, \tau_{\text{D}_{\text{pel}}}^{\text{lag}}, \tau_{\text{DT}_{\text{pel}}}^{\text{lag}})$ is a diagonal matrix whose elements are time constants that represent the lag in actuation. These time constants are considered to be uncertain (not known).

All of the time constants are assumed to be proportional to the aforementioned plasma response times from [11] except for $\tau_{\text{nbi}_1}^{\text{lag}}$. The time constant for the NBI actuators is the sum of the plasma response time (~ 80 ms) and the more significant NBI thermalization delay. In the plasma, an NBI ion loses energy, ε_{nbi} , at a rate of

$$\frac{d\varepsilon_{\text{nbi}}}{dt} = -B\varepsilon_{\text{nbi}} - B\varepsilon_{\text{nbi}}(\varepsilon_c/\varepsilon_{\text{nbi}})^{3/2}, \quad (26)$$

where $B = e^4 n_e m_e^{\frac{1}{2}} Z_{\text{nbi}}^2 \ln \Lambda_e / (3\sqrt{2}\pi^{\frac{3}{2}} \varepsilon_0^2 m_{\text{nbi}} T_e^{\frac{3}{2}})$ [6, 20]. For ITER, the NBI ion's charge Z_{nbi} and mass m_{nbi} are that of a D ion. The NBI thermalization delay can be found by integrating (26) from zero to the thermalization delay. For the plasma conditions considered in section 10, this thermalization delay is approximately ~ 0.5 s.

8. Nonadaptive, static actuator allocator

The control laws derived in section 5 represent the stabilizing virtual control efforts $v_s = [P_{\text{aux},i}^{\text{stable}} P_{\text{aux},e}^{\text{stable}} S_{\text{D}}^{\text{stable}} S_{\text{T}}^{\text{stable}}]^T$. In a modular design, the requested virtual control efforts v_s are sent from the controller to the actuator allocator. The actuator allocator attempts to achieve v_s using the available actuators. The virtual control efforts actually produced by the actuators are denoted as $v = [P_{\text{aux},i} P_{\text{aux},e} S_{\text{D}} S_{\text{T}}]^T$. The allocator attempts to drive the allocation error $|v_s - v|$ to zero.

In this section, the actuator allocator designed in the authors' prior work [9] is presented. This work combines this allocation algorithm with the controller presented in section 5 to create one of the two burn control schemes that will be evaluated in a simulation study (section 10). This actuator allocator is designed with the assumptions that the effector model (section 6) does not contain any uncertainty and that there are no actuator dynamics (section 7). The parameter vector θ_e is assumed to be known, and the actuation is assumed to be instantaneous ($u_d = u_{\text{cmd}} = u$ always). Recalling figure 1, this allocator assumes that its output u_d skips the two blocks for the low-level actuator control algorithm and the actuator dynamics. Therefore, u_d enters directly into the block for the effector

model (a component of the plasma system). Figure 2 describes this simplified closed-loop model.

Since there are four heating actuators (P_{ic} , P_{ec} , P_{nbi_1} and P_{nbi_2}) and two virtual control efforts for plasma heating ($P_{\text{aux},i}$ and $P_{\text{aux},e}$) in (24), ITER is overactuated in regard to its power systems [28]. The actuator allocation algorithm presented in this section will attempt to reproduce the desired virtual control efforts for power using the available ITER heating actuators. The algorithm considers actuator saturation and rate constraints. The effector model (24) for the auxiliary power is rewritten as

$$\begin{aligned} v^* &= Bu^* = \begin{bmatrix} \eta_{\text{ic}} & 0 & \eta_{\text{nbi}_1} \phi_{\text{nbi}} & \eta_{\text{nbi}_2} \phi_{\text{nbi}} \\ 0 & \eta_{\text{ec}} & \eta_{\text{nbi}_1} \bar{\phi}_{\text{nbi}} & \eta_{\text{nbi}_2} \bar{\phi}_{\text{nbi}} \end{bmatrix} u^*, \\ v^* &= [P_{\text{aux},i} \ P_{\text{aux},e}]^T, \quad u^* = [P_{\text{ic}} \ P_{\text{ec}} \ P_{\text{nbi}_1} \ P_{\text{nbi}_2}]^T, \end{aligned} \quad (27)$$

where vectors u^* and v^* are, respectively, truncations of the u and v vectors that were previously defined in section 6. They exclude the external fueling terms ($S_{\text{D}_{\text{pel}}}$, $S_{\text{DT}_{\text{pel}}}$, S_{D} and S_{T}) because ITER's fueling systems are not overactuated when gas injection is omitted. For the core plasma, the fueling efficiency from gas injection is predicted to be less than 1% in ITER [10, 29]. The commands for the pellet injectors can be solved directly from (24):

$$S_{\text{DT}_{\text{pel}}} = \frac{S_{\text{T}}}{\eta_{\text{DT}_{\text{pel}}} \gamma_{\text{DT}_{\text{pel}}}}, \quad (28)$$

$$S_{\text{D}_{\text{pel}}} = \frac{S_{\text{D}} - \eta_{\text{DT}_{\text{pel}}} (1 - \gamma_{\text{DT}_{\text{pel}}}) S_{\text{DT}_{\text{pel}}}}{\eta_{\text{D}_{\text{pel}}}}. \quad (29)$$

The actuator allocation problem for ITER's heating systems can be posed as a quadratic program [12]:

$$\begin{aligned} &\underset{s, u^*}{\text{minimize}} \quad \left(\sum_{i=1}^2 g_i s_i^2 + \sum_{j=1}^4 w_j (u_j^*)^2 \right) \\ &\text{subject to} \quad Bu^* = v^* + s, \quad u_i^* \leq u^* \leq \bar{u}_i^*, \end{aligned} \quad (30)$$

where the primary objective is to minimize the slack variables $s = [s_1, s_2]^T$ (thereby minimizing the error in the mapping between u^* and v^*), and the secondary objective is to minimize power consumption. This secondary objective also improves the numerical conditioning of matrix H which is introduced below for the rewritten optimization problem (32). The elements of g and w are weights that are selected to prioritize the primary objective. The most restrictive lower and upper actuator constraints at each time step are given by

$$u_l^* = \max(\underline{u}^*, u_{\Delta}^* + \Delta t \underline{\delta}), \quad u_u^* = \min(\bar{u}^*, u_{\Delta}^* + \Delta t \bar{\delta}), \quad (31)$$

where \underline{u}^* and \bar{u}^* contain the lower and upper actuator saturation constraints, $\underline{\delta}$ and $\bar{\delta}$ contain the lower and upper actuator rate constraints, and u_{Δ}^* is u^* from the previous time step.

The quadratic program (30) can be put into as the standard form [30] by defining $H = 2 \times \text{diag}(w_1, \dots, w_4, g_1, g_2)$ where

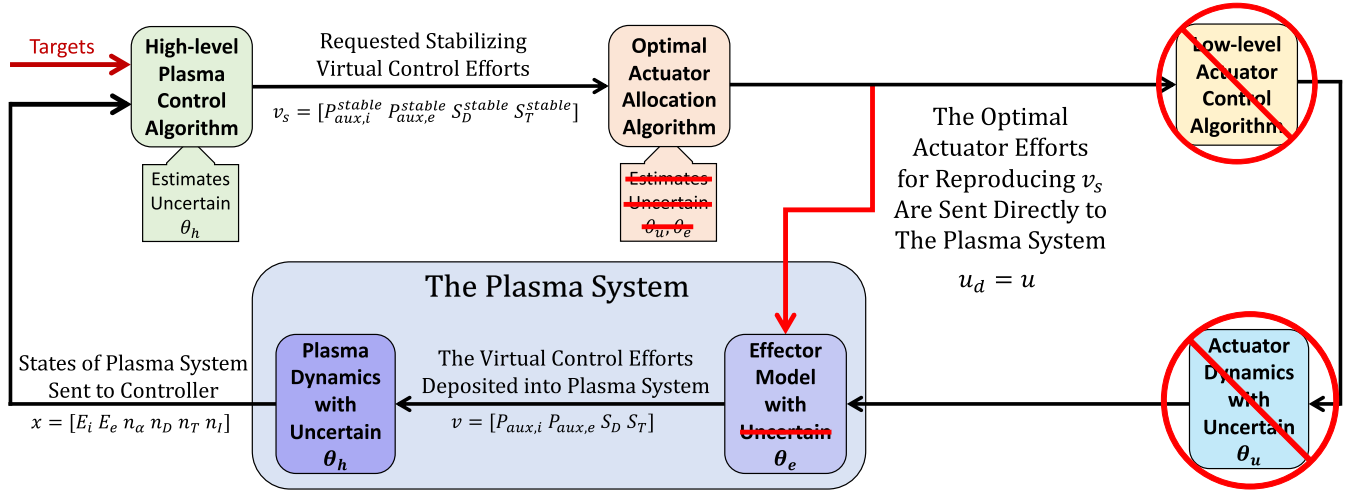


Figure 2. The actuator allocation algorithm presented in section 8 was designed for the closed-loop plasma system represented by the above flow chart. This closed-loop system assumes that there are no actuator dynamics and that the mapping between the actuation efforts u and the virtual control efforts v contains no uncertainty (θ_h is known and $u = u_d$).

H is positive definite. The resulting optimization problem is strictly convex:

$$\begin{aligned} & \underset{s, u^*}{\text{minimize}} && \frac{1}{2} (u^{*T}, s^T) H \begin{pmatrix} u^* \\ s \end{pmatrix} \\ & \text{subject to} && (B, -I) \begin{pmatrix} u^* \\ s \end{pmatrix} = v^*, \\ & && \begin{pmatrix} I & 0 \\ -I & 0 \end{pmatrix} \begin{pmatrix} u^* \\ s \end{pmatrix} \geq \begin{pmatrix} u_i^* \\ -u_i^* \end{pmatrix}. \end{aligned} \quad (32)$$

9. Adaptive, dynamic actuator allocator

In this section, the new adaptive, dynamic allocator that is designed for the closed-loop system shown in figure 1 is presented. To make the design of the allocation algorithm [17] easier, the high-level dynamics (1), (2), (4) through (7), the effector model (24), and the actuator dynamics (25) are put into a more generalized form. The high-level dynamics are rewritten as $\dot{x} = f(x) + g(x)v$ where $x = [E_i \ E_e \ n_\alpha \ n_D \ n_T \ n_I]^T$. Both $f(x)$ and $g(x)$ are easily inferred (θ_h is incorporated into $f(x)$). The effector model (24) and actuator dynamics (25) are rewritten as

$$\begin{aligned} v &= \Phi(u, \theta_e) = \Phi_{\theta_e}(u)\theta_e, \\ \dot{u} &= f_{\theta_u}(u, u_{\text{cmd}})\theta_u, \\ \theta_u &= \left[1/\tau_{ic}^{\text{lag}} \quad 1/\tau_{ec}^{\text{lag}} \quad 1/\tau_{nbi}^{\text{lag}} \quad 1/\tau_{pel}^{\text{lag}} \right]^T, \\ \theta_e &= [\theta_{e1} \ \theta_{e2}]^T, \\ \theta_{e1} &= [\eta_{ic} \ \eta_{nbi1} \ \phi_{nbi} \ \eta_{nbi2} \ \phi_{nbi} \ \eta_{ec} \ \eta_{nbi1} \ \eta_{nbi2}]^T, \\ \theta_{e2} &= [\eta_{D_{pel}} \ \eta_{DT_{pel}} \ \eta_{DT_{pel}} \ \gamma_{DT_{pel}}]^T. \end{aligned} \quad (33)$$

The vectors θ_e and θ_u lump together the uncertain parameters. The proposed allocator's estimates of the uncertain parameters

are denoted as $\hat{\theta}_e$ and $\hat{\theta}_u$. The $\Phi(u, \theta_e)$, Φ_{θ_e} and $f_{\theta_u}(u, u_{\text{cmd}})$ matrices can be easily inferred from the effector model (24) and the actuator dynamics (25). In this generalized formulation, v is the output, x and u are measured, and u_{cmd} is the controlled input.

The actuator allocation algorithm takes the desired virtual control reference v_s as an input from the controller and dynamically computes the desired actuator reference u_d as an output. The desired virtual control reference v_s is the vector of stabilizing controls calculated by the high-level controller from (19)–(22). The goal of the allocation algorithm is to get the actual virtual control efforts v from the effector model (24) to match the reference v_s by dynamically updating reference u_d . The low-level control u_{cmd} will attempt to bring the actual actuation efforts u to the computed value of reference u_d . The reference u_d is the argument of the minimization problem:

$$\begin{aligned} & \underset{u_d}{\text{minimize}} && J(u_d) \\ & \text{subject to} && v_s - \Phi(u_d + \tilde{u}, \hat{\theta}_e) = 0, \end{aligned} \quad (34)$$

where $\tilde{u} = u - u_d$ and $J(u_d)$ is the cost function. For the proposed dynamic allocator, each of the following cost functions can be used for $J(u_d)$

$$J_1(u_d) = z(\text{diag}(u_d)u_d), \quad (35)$$

$$\begin{aligned} J_2(u_d) &= z(\text{diag}(u_d)u_d) - \sum_{i=1}^6 q_i \log(\bar{u}_i - u_{d,i}) \\ &\quad - \sum_{j=1}^6 m_j \log(u_{d,j}), \end{aligned} \quad (36)$$

where z^T , q^T and m^T are column vectors filled with weighting constants. Recall that \bar{u} is the vector of upper saturation limits for each actuator. The first cost function (35) only seeks to minimize the actuation effort, while the second cost function (36) takes into account the actuator saturation limits by using

barrier functions. Recall that the upper and lower saturation limits are given by \bar{u} and $\underline{u} = 0$, respectively.

By introducing a Lagrangian function with Lagrangian parameter vector λ , the constrained optimization problem (34) can be written as an unconstrained optimization problem, i.e.

$$L(u_d, \tilde{u}, \lambda, \hat{\theta}_e, \hat{\theta}_u) = J(u_d) + (v_s - \Phi(u_d + \tilde{u}, \hat{\theta}_e))^T \lambda, \quad (37)$$

$$\underset{u_d, \lambda}{\text{minimize}} \quad L(u_d, \tilde{u}, \lambda, \hat{\theta}_e, \hat{\theta}_u). \quad (38)$$

Based on [17], update laws for u_d , λ , $\hat{\theta}_e$ and $\hat{\theta}_u$ are developed to conserve the stability of the closed-loop system (1), (2), (4) through (7), (24) and (25). Two observers are employed for the adaptive estimation scheme of the uncertain (not known) parameters (θ_u and θ_e). With Hurwitz matrices $A_{\hat{u}}$ and $A_{\hat{x}}$, the two observers are

$$\dot{\hat{u}} = A_{\hat{u}}(\hat{u} - u) + f_{\theta_u}(u, u_{\text{cmd}})\hat{\theta}_u, \quad (39)$$

$$\dot{\hat{x}} = A_{\hat{x}}(\hat{x} - x) + f(x) + g(x)\Phi(u, \hat{\theta}_e). \quad (40)$$

The four update laws for the adaptive allocation algorithm are defined by

$$\begin{pmatrix} \dot{u}_d \\ \dot{\lambda} \end{pmatrix} = -\Gamma H \begin{pmatrix} \frac{\partial L}{\partial u_d} \\ \frac{\partial L}{\partial \lambda} \end{pmatrix} - u_{ff}, \quad (41)$$

$$u_{ff} = H^{-1} \begin{pmatrix} \frac{\partial^2 L}{\partial \tilde{u} \partial u_d} \\ \frac{\partial^2 L}{\partial \tilde{u} \partial \lambda} \end{pmatrix} f_{\tilde{u}}(\tilde{u}, u_d, u_{\text{cmd}}, \hat{\theta}_u) + H^{-1} \begin{pmatrix} \frac{\partial^2 L}{\partial \hat{\theta} \partial u_d} \\ \frac{\partial^2 L}{\partial \hat{\theta} \partial \lambda} \end{pmatrix} \dot{\hat{\theta}},$$

$$H = \begin{pmatrix} \frac{\partial^2 L}{\partial u_d^2} & \frac{\partial^2 L}{\partial \lambda \partial u_d} \\ \frac{\partial^2 L}{\partial u_d \partial \lambda} & 0 \end{pmatrix},$$

$$\dot{\hat{\theta}}_e^T = \xi_x^T \Gamma_x g(x) \Phi_{\theta_e}(u) \Gamma_{\theta_e}^{-1},$$

$$\begin{aligned} \dot{\hat{\theta}}_u^T &= \left(\frac{\partial V_{\tilde{u}}}{\partial \tilde{u}} + \xi_u^T \Gamma_u \right) f_{\theta_u}(u, u_{\text{cmd}}) \Gamma_{\theta_u}^{-1} \\ &+ \left(\xi_x^T \Gamma_x + \frac{\partial L^T}{\partial u_d} \frac{\partial^2 L}{\partial \tilde{u} \partial u_d} + \frac{\partial L^T}{\partial \lambda} \frac{\partial^2 L}{\partial \tilde{u} \partial \lambda} \right) f_{\theta_u}(u, u_{\text{cmd}}) \Gamma_{\theta_u}^{-1}, \end{aligned}$$

where $\hat{\theta} \triangleq (\hat{\theta}_u^T, \hat{\theta}_e^T)^T$, $\xi_u \triangleq u - \hat{u}$, $\xi_x \triangleq x - \hat{x}$, and Γ , Γ_{θ_u} , Γ_{θ_e} , Γ_u and Γ_x are symmetric positive definite matrices. In contrast to the dynamic allocator (41), the static allocator incorporates the hard constraints for the actuator limits in the optimization problem (32) instead of using barrier functions as in (36), avoiding in this way the tuning of the cost-function weights associated with the barrier functions.

Because of the actuator dynamics described in section 7, a low-level controller is designed. The low-level control u_{cmd} is manipulated in an attempt to force the actual actuation effort u , which is determined by the actuator dynamics (25), to the desired actuation effort u_d that is calculated using (41). Since

the dynamics of all of the actuators take the same form (25), each actuator's low-level control law will have the same form. The control for each actuator is developed using the Lyapunov functions

$$V_{\tilde{u},i} = \frac{\tilde{u}_i^2}{2} \quad \text{for } i \in \{1, \dots, 6\}, \quad (42)$$

where each $V_{\tilde{u},i}$ depends on the i th element of $\tilde{u} = [\tilde{P}_{\text{ic}} \tilde{P}_{\text{ec}} \tilde{P}_{\text{nb}1} \tilde{P}_{\text{nb}2} \tilde{S}_{\text{Dpel}} \tilde{S}_{\text{DTpel}}]^T$. Using the procedure shown in appendix C, the control law for each actuator is formulated as

$$u_{\text{cmd},i} = u_{d,i} + \frac{\dot{u}_{d,i}}{\hat{\Theta}_{u,i}} \quad \text{for } i \in \{1, \dots, 6\}, \quad (43)$$

$$\hat{\Theta}_u = [\hat{\theta}_{u,1} \quad \hat{\theta}_{u,2} \quad \hat{\theta}_{u,3} \quad \hat{\theta}_{u,3} \quad \hat{\theta}_{u,4} \quad \hat{\theta}_{u,4}]^T, \quad (44)$$

where $u_{d,i}$ and $\hat{\theta}_{u,i}$ refer to the i th element of u_d and $\hat{\theta}_u$, respectively. The elements of $\hat{\Theta}_u$ can be readily inferred from the elements of θ_u (33) and the actuator dynamics (25). The Lyapunov functions $V_{\tilde{u},i}$ and $\dot{u}_i = f_{\tilde{u}_i}(\tilde{u}_i, u_{d,i}, u_{\text{cmd},i}, \hat{\Theta}_{u,i})$ for $i \in \{1, \dots, 6\}$ are put into vectors $V_{\tilde{u}}$ and $f_{\tilde{u}}$ for use in the adaptive, dynamic allocation algorithm (41).

10. Simulation study

The following simulation study is an assessment of the burn control algorithm presented in section 5 augmented with each of the two actuator allocation algorithms presented in sections 8 and 9. The results of five different simulations are reviewed. The following information is common to all five simulations. The initial conditions are set to $n_\alpha = 2 \times 10^{18} \text{ m}^{-3}$, $n_D = 3 \times 10^{19} \text{ m}^{-3}$, $n_T = 3 \times 10^{19} \text{ m}^{-3}$, $n_I = 1 \times 10^{18} \text{ m}^{-3}$, $E_i = 1.5 \times 10^5 \text{ J m}^{-3}$ and $E_e = 1.8 \times 10^5 \text{ J m}^{-3}$. Because the beryllium source from wall sputtering could be significant in ITER [31], $Z_I = 4$ for Be is chosen in this study (any other choice like a weighted average between the atomic numbers of Be and W, for instance, is possible). Parameters in the plasma model are set to $H_H = 1$, $\zeta_i = 1.1$, $\zeta_e = 0.9$, $k_D = 3$, $k_T = 2$, $k_\alpha = 4$, $k_I = 6$, $\phi_\alpha = 0.15$, $f_{\text{eff}} = 0.1$, $f_{\text{ref}} = 0.5$, $R^{\text{eff}} = 0.6$, $\gamma^{\text{PFC}} = 0.5$ and $f_1^{\text{sp}} = 0.01$. The upper saturation limits of ITER's actuators [11] are $P_{\text{ic}}^{\text{max}} = 20 \text{ MW}$, $P_{\text{ec}}^{\text{max}} = 20 \text{ MW}$, $P_{\text{nb}1}^{\text{max}} = 16.5 \text{ MW}$, $P_{\text{nb}2}^{\text{max}} = 16.5 \text{ MW}$, $S_{\text{Dpel}}^{\text{max}} = 120 \text{ Pa m}^3 \text{ s}^{-1}$ and $S_{\text{DTpel}}^{\text{max}} = 111 \text{ Pa m}^3 \text{ s}^{-1}$. The lower saturation limits of all of the actuators are set to zero. For the power actuators, the rate constraints are all set to $\pm 10 \text{ MW s}^{-1}$.

The simulation study is broken up into scenarios A–C. Scenario A covers the first two simulations, scenario B covers the third simulation, and scenario C covers the last two simulations. In scenario A, the performances of the controller (19)–(22) with and without adaptive estimation of the uncertain plasma parameters (23) are compared (θ_h is not known). These two simulations assume that the parameters in the effector model are certain ($\hat{\theta}_e = \theta_e$ always), and they assume that there are no actuator dynamics ($u_d = u$ as depicted in figure 2). The nonadaptive, static allocator (32) is used with the adaptive and nonadaptive controllers in scenario A. In contrast, the adaptive, dynamic allocator (41) with cost function $J_1(u_d)$ (35)

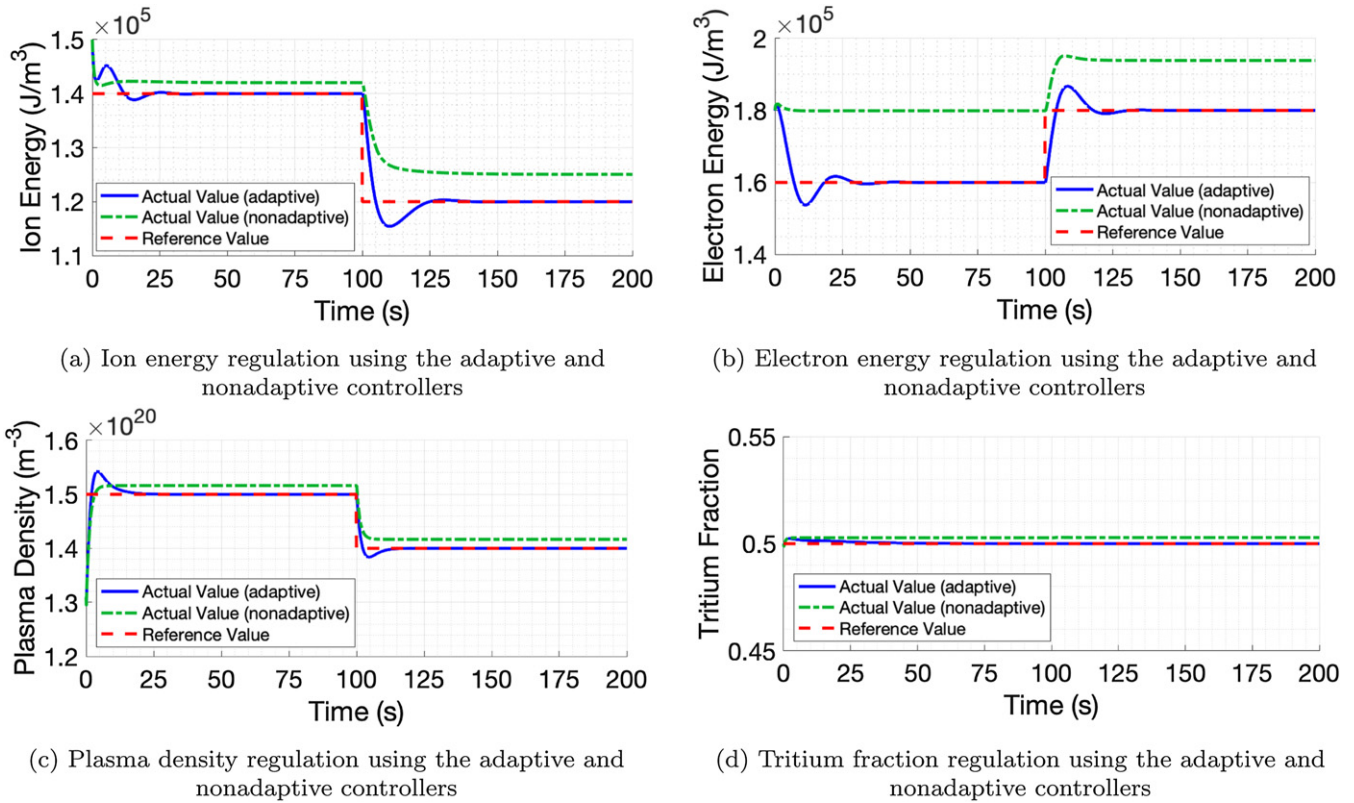


Figure 3. Scenario A—simulation results are for the adaptive (blue-solid lines) and nonadaptive (green-dash-dot lines) controllers augmented with the *nonadaptive, static allocator*. The burn control schemes attempt to bring the ion energy, electron energy, plasma density and tritium fraction to their desired values (red-dashed lines). For scenario A, there is uncertainty in the plasma model (θ_h is not known), all parameters in the effector model are known (θ_e is known), and actuator dynamics are not included (instantaneous actuation). Because of the uncertainties present in the plasma model, the nonadaptive controller fails to track the desired targets while the adaptive controller succeeds.

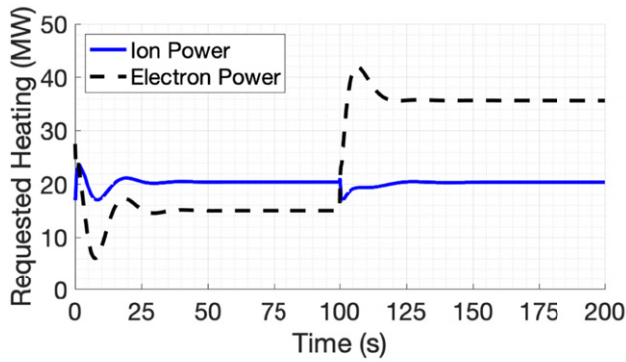
is evaluated in scenario B. In scenario B, the adaptive controller is used and the parameters for the effector model and the actuator dynamics (θ_e and θ_u) are not known (actuator dynamics are included as depicted in figure 1). In scenario C, the targets (i.e. reference or desired values) that are sent to the controller, the parameters in the effector model (θ_e), and the initial estimates of all of the uncertain parameters (θ_h , θ_e and θ_u) are different from scenarios A and B. With the two simulations for scenario C, the cost function $J_1(u_d)$ (35) is compared to the cost function $J_2(u_d)$ (36) for use in the adaptive, dynamic allocator's Lagrangian function.

10.1. Scenario A: nonadaptive, static allocation

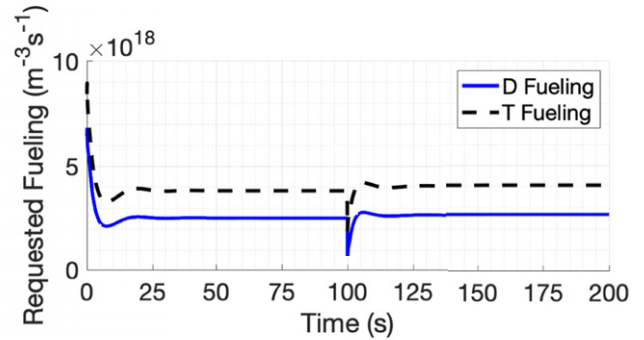
Two simulations are performed for scenario A which assumes that there are no actuator dynamics. In the effector model, the parameters are set to $\eta_{ic} = 0.9$, $\eta_{ec} = 0.92$, $\eta_{nbi_1} = 1$, $\eta_{nbi_2} = 0.95$, $\eta_{Dpel} = 0.93$, $\eta_{DTpel} = 1$, $\gamma_{DTpel} = 0.9$ and $\phi_{nbi} = 0.2$. At the start of each simulation, the desired equilibrium point sent to the controller is the solution of (16) with $d/dt = 0$ when $\bar{E}_i = 1.4 \times 10^5 \text{ J m}^{-3}$, $\bar{E}_e = 1.6 \times 10^5 \text{ J m}^{-3}$, $\bar{n} = 1.5 \times 10^{20} \text{ m}^{-3}$ and $\bar{\gamma} = 0.5$. After 100 s in each simulation, the desired equilibrium point changes to the solution of (16) with $d/dt = 0$ when $\bar{E}_i = 1.2 \times 10^5 \text{ J m}^{-3}$, $\bar{E}_e = 1.8 \times 10^5 \text{ J m}^{-3}$, $\bar{n} = 1.4 \times 10^{20} \text{ m}^{-3}$ and $\bar{\gamma} = 0.5$. The initial estimate of the uncertain vector $\hat{\theta}_h$ is calculated by multiplying the nominal values of each element, in order, with

the following numbers: 1.09, 1.05, 0.95, 0.9, 0.92, 0.96, 1.07, 1.04, 1.10, 0.88, 0.92 and 1.08. The effector model parameters are considered to be known such that adaptive estimation of θ_e is not needed. Without actuator dynamics, θ_u is irrelevant.

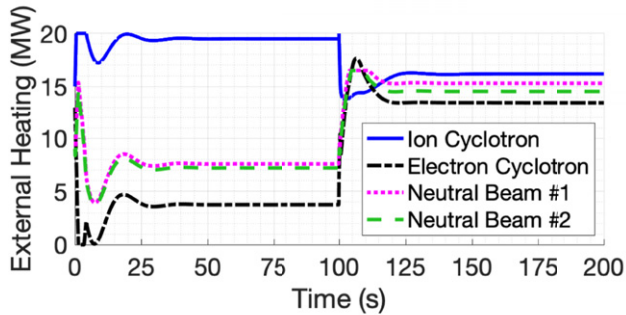
For scenario A, the performance of the adaptive controller defined by (19)–(23) is compared to the performance of the controller with adaptive estimation turned off ($\dot{\theta} = 0$). The nonadaptive, static allocator presented in section 8 is used in the two simulations. The results of the two simulations are shown in figures 3 and 4. As seen in figures 3(a)–(d), the adaptive controller with the nonadaptive, static allocator (blue-solid lines) successfully tracks the desired targets (red-dashed lines) for the ion energy, electron energy, plasma density and tritium fraction despite the uncertainty in the plasma confinement, DT wall recycling, impurity sputtering and the alpha particle ion-heating fraction. When the controller requests the external heating and fueling shown in figures 4(a) and (b), the allocator successfully commands the ion cyclotron system, electron cyclotron system, neutral beam injectors and pellet injectors in order to optimally reproduce these virtual control efforts (figures 4(c) and (d)). Without adaptive estimation, the controller fails to meet the control objectives provided in section 4 (see the green-dash-dot lines in figure 3). Figures 4(e)–(h) show the virtual control and actuation efforts produced by the nonadaptive controller with nonadaptive, static allocation. Comparing figure 4(e) to figure 4(a), it can be seen that the



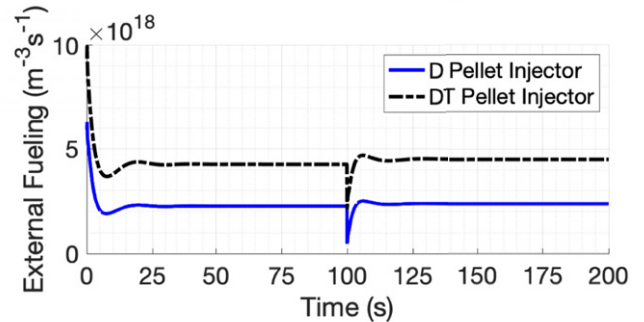
(a) Stabilizing ion and electron heating requested by the **adaptive** controller



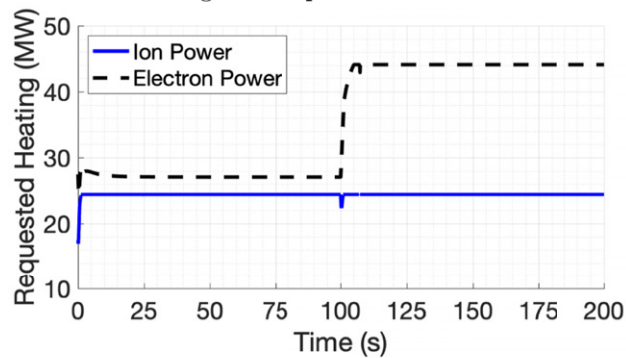
(b) Stabilizing deuterium and tritium fueling requested by the **adaptive** controller



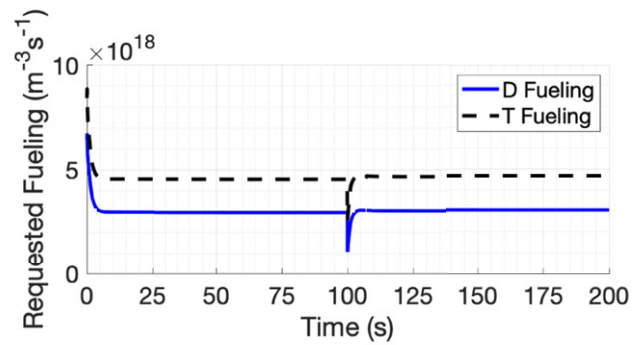
(c) Actuator heating efforts sent to plasma system when using the **adaptive** controller



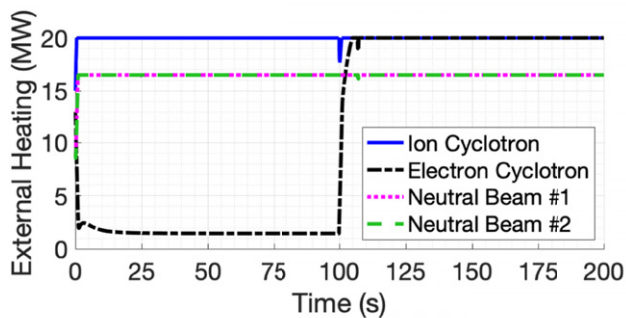
(d) Actuator fueling efforts sent to plasma system when using the **adaptive** controller



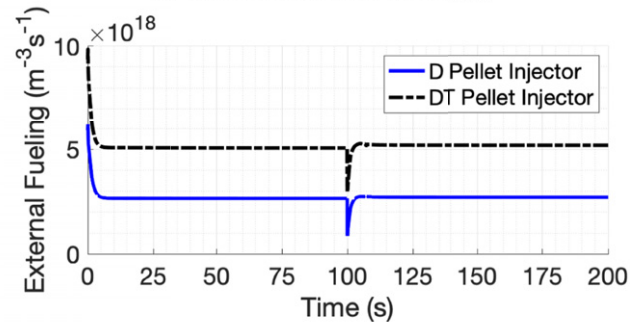
(e) Stabilizing ion and electron heating requested by the **nonadaptive** controller



(f) Stabilizing deuterium and tritium fueling requested by the **nonadaptive** controller



(g) Actuator heating efforts sent to plasma system when using the **nonadaptive** controller



(h) Actuator fueling efforts sent to plasma system when using the **nonadaptive** controller

Figure 4. Scenario A—simulation results in (a)–(d) are for the adaptive controller augmented with the *nonadaptive, static allocator*. Simulation results with adaptive estimation turned off are given in (e)–(h). The controller requests the external ion power and electron power shown in (a) (or (e)), and it requests the external deuterium and tritium fueling shown in (b) (or (f)). After receiving instructions from the allocator, the ion cyclotron system, electron cyclotron system, neutral beam injectors and pellet injectors produce the actuation efforts shown in (c) and (d) (or (g) and (h)).

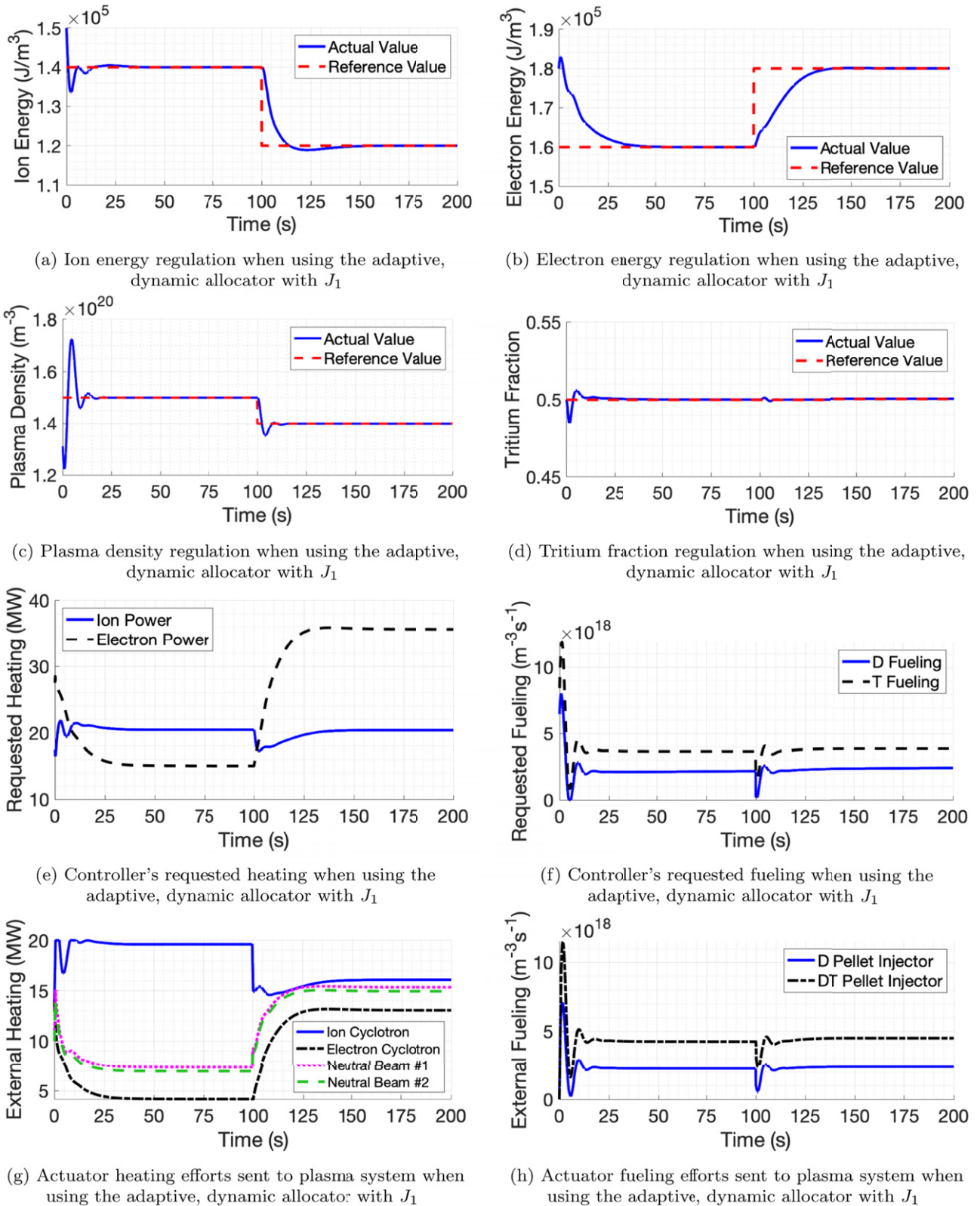


Figure 5. Scenario B—simulation results for the adaptive controller augmented with the *adaptive, dynamic allocator*. The adaptive, dynamic allocator's algorithm uses cost function J_1 (35). The burn control scheme successfully drives the ion energy (a), electron energy (b), plasma density (c) and tritium fraction (d) to their desired values. The controller requests the external ion and electron powers shown in (e), and it requests the deuterium and tritium fueling shown in (f). After receiving instructions from the allocator, the ion cyclotron system, electron cyclotron system, neutral beam injectors and pellet injectors produce the actuation efforts shown in (g) and (h). For scenario B, there is uncertainty in the plasma model, the effector model and the actuator dynamics (θ_h , θ_e and θ_u are not known).

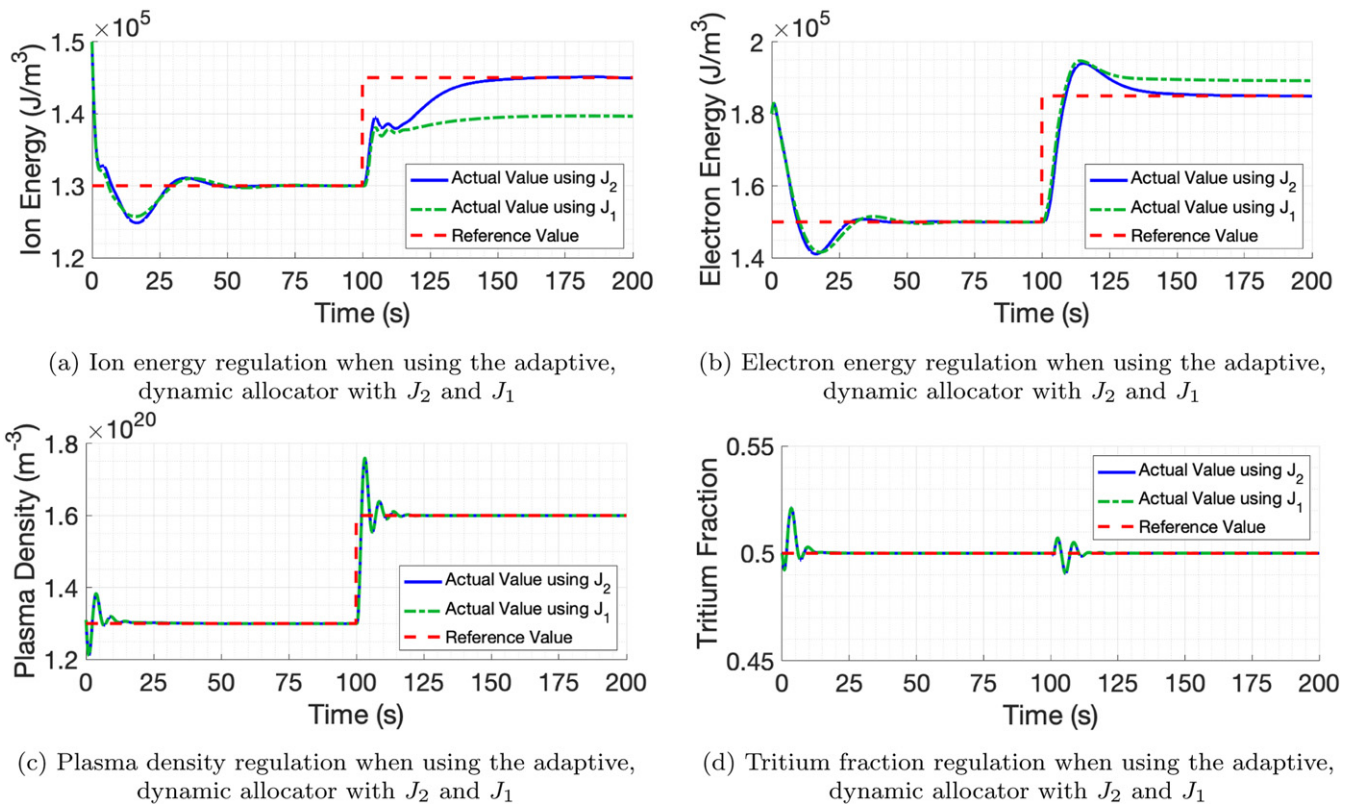


Figure 6. Scenario C—results from two simulations that both use the adaptive controller augmented with the *adaptive, dynamic allocator*. In the simulation represented with the blue-solid lines, the allocator used cost function J_2 (36) which includes the actuator constraints as barrier functions. In the simulation represented by the green-dash-dot lines, the allocator used the cost function J_1 (35) which does not consider the actuator constraints. The burn control schemes attempt to bring the ion energy, electron energy, plasma density and tritium fraction to their desired values (red-dashed lines). For scenario C, there is uncertainty in the plasma model, the effector model and the actuator dynamics (θ_n , θ_e and θ_u are not known).

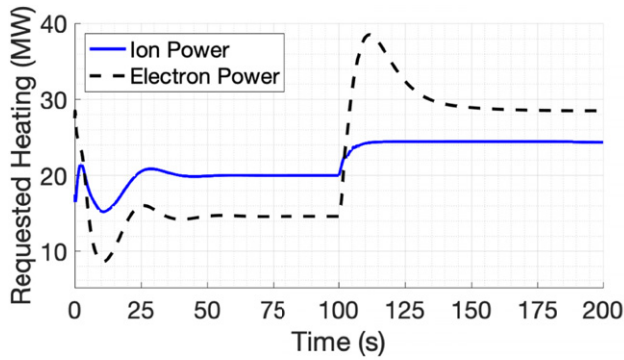
nonadaptive controller requests too much auxiliary heating. As a result, the power actuators needlessly reach their upper saturation limit (figure 4(g)). These simulations clearly illustrate the importance of the burn controller's adaptive estimation scheme.

10.2. Scenario B: adaptive, dynamic allocation

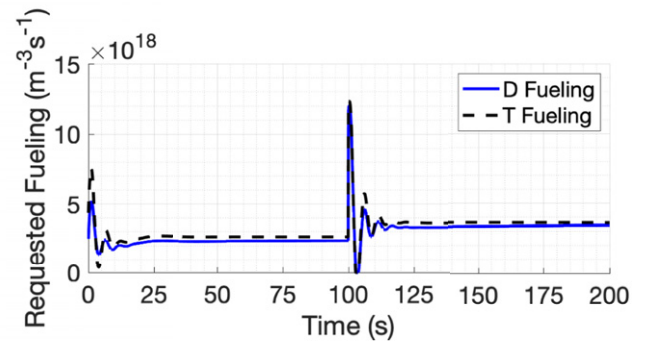
Scenario B uses the same controller targets and initial estimate of uncertain vector $\hat{\theta}_n$ as scenario A. For scenario B, the effector model contains uncertainty ($\hat{\theta}_e \neq \theta_e$) and the uncertain actuator dynamics described in section 7 are included ($\hat{\theta}_u \neq \theta_u$). In the effector model, the parameters are set to $\eta_{ic} = 0.9$, $\eta_{ec} = 0.92$, $\eta_{nbi_1} = 1$, $\eta_{nbi_2} = 0.95$, $\eta_{Dpel} = 0.93$, $\eta_{DTpel} = 1$, $\gamma_{DTpel} = 0.9$ and $\phi_{nbi} = 0.2$ (same as scenario A). Respectively, the time constants τ_{ic}^{lag} , τ_{ec}^{lag} , τ_{nbi}^{lag} and τ_{pel}^{lag} are set to 5×0.2 , 5×0.02 , 5×0.58 and 5×0.1 s. To evaluate robustness, the time constants were chosen to be a five-fold increase of the nominal plasma response times reported in section 7. The initial estimate of the uncertain vector $\hat{\theta} \triangleq (\hat{\theta}_u^T, \hat{\theta}_e^T)^T$ is calculated by multiplying the nominal values of each element, in order, with the following numbers: 1.07, 1.18, 1.11, 0.95, 1.16, 0.95, 0.89, 1.05, 1.11, 1.14, 0.92, 0.92 and 0.95.

For scenario B, only one simulation is performed and the results are shown in figure 5. In this simulation, the adaptive controller with the adaptive, dynamic allocation (41) (see section 9) is used. The simpler cost function J_1 (35) is used for the allocator's optimization algorithm. Figure 5 shows that this burn control scheme can successfully track desired equilibria despite the nonzero actuation lag ($T_{lag} \neq 0$) and the uncertainty introduced in the plasma model, the effector model (24) and the actuator dynamics (25). In figures 5(e) and (f), the stabilizing virtual control efforts v_s that are requested by the controller are shown. Figures 5(g) and (h) plot the low-level control u_{cmd} , which is calculated using the control law (43), that brings the actual (lagged) actuation efforts u , which are mapped back to virtual control efforts v in (24), to the desired actuation effort u_d . The u_d vector is optimally calculated using the allocator's dynamic update laws (41), and it successfully reproduces v_s .

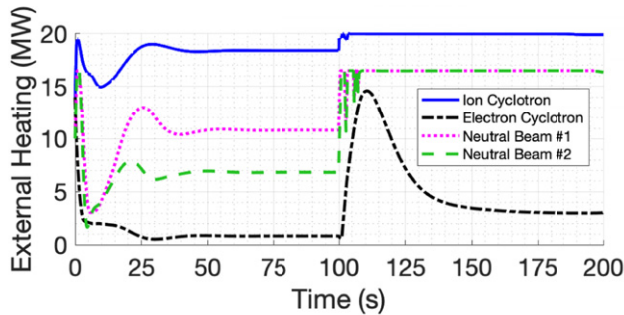
The computational performances of the nonadaptive, static allocator and the adaptive, dynamic allocator can now be compared. For the simulation of scenario A with the adaptive controller, the execution of the static allocation algorithm accounted for 67.7% of the simulation time, while the execution of the dynamic allocation algorithm in the scenario B simulation accounted for only 39.6% of the simulation time. The total run time of the simulation with the nonadaptive, static



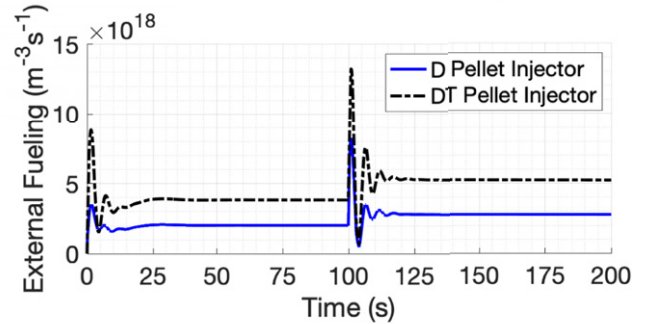
(a) Controller's requested heating when using the adaptive, dynamic allocator with J_2



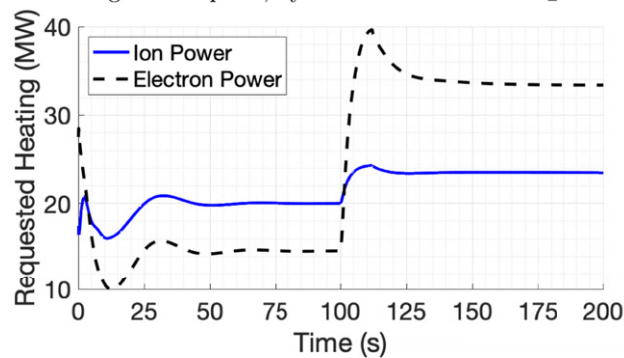
(b) Controller's requested fueling when using the adaptive, dynamic allocator with J_2



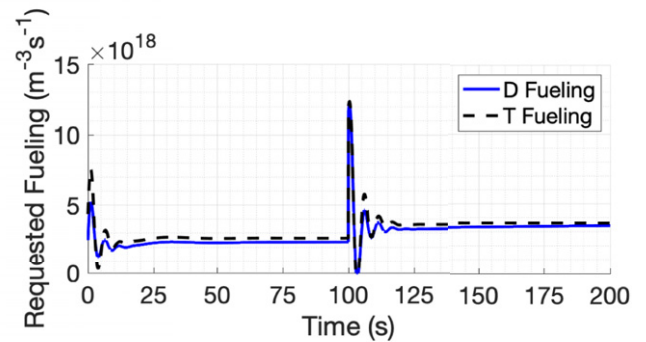
(c) Actuator heating efforts sent to plasma system when using the adaptive, dynamic allocator with J_2



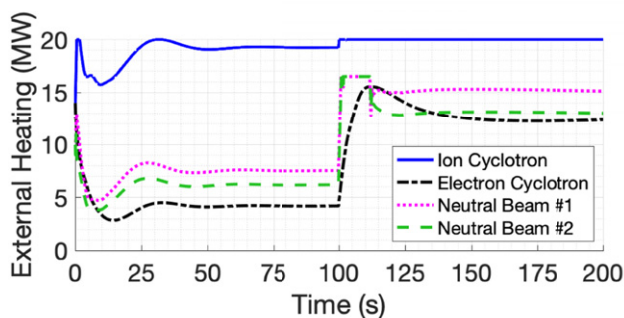
(d) Actuator fueling efforts sent to plasma system when using the adaptive, dynamic allocator with J_2



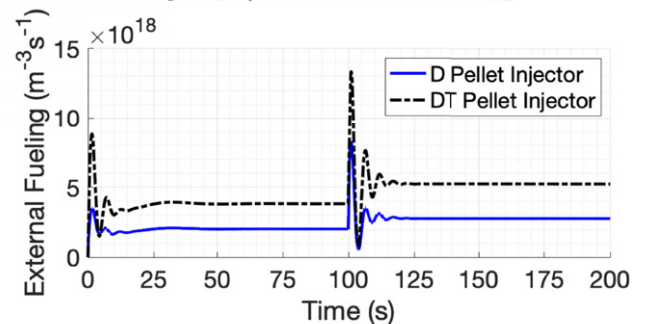
(e) Controller's requested heating when using the adaptive, dynamic allocator with J_1



(f) Controller's requested fueling when using the adaptive, dynamic allocator with J_1



(g) Actuator heating efforts sent to plasma system when using the adaptive, dynamic allocator with J_1



(h) Actuator fueling efforts sent to plasma system when using the adaptive, dynamic allocator with J_1

Figure 7. Scenario C—simulation results in (a)–(d) are for the adaptive controller augmented with the *adaptive, dynamic allocator* that uses cost function J_2 (36). The results shown in (e)–(h) are for the simulation that uses the cost function J_1 (36) instead of J_2 for the allocator. Unlike J_1 , the cost function J_2 considers the actuator constraints. The controller requests the external power and fueling shown in (a) and (b) (or (e) and (f)), respectively. Based on instructions from the allocator, the ion cyclotron system, electron cyclotron system, neutral beam injectors and pellet injectors produce the actuation efforts shown in (c) and (d) (or (g) and (h)).

allocator was approximately 2.5 times longer than the total run time of the simulation with the adaptive, dynamic allocator. As expected, the dynamic allocator is more computationally efficient.

10.3. Scenario C: comparing cost functions

In scenario C, the plasma model, the effector model and the actuator dynamics contain uncertainty ($\hat{\theta}_h \neq \theta_h$, $\hat{\theta}_e \neq \theta_e$ and $\hat{\theta}_u \neq \theta_u$). This scenario is used to evaluate the adaptive, dynamic allocator (with the adaptive controller) when it is based on each of the cost functions J_1 (35) and J_2 (36). The second cost function, J_2 , is more complex than the first cost function, J_1 , because it includes the actuator saturation limits as barrier functions. In scenario C, the controller's targets, the effector model's θ_e , and the initial estimates of θ_h , θ_e and θ_u differ from scenarios A and B. At the beginning of the simulation, the controller's targets are defined by the solution of (16) with $d/dt = 0$ when $\bar{E}_i = 1.3 \times 10^5 \text{ J m}^{-3}$, $\bar{E}_e = 1.5 \times 10^5 \text{ J m}^{-3}$, $\bar{n} = 1.3 \times 10^{20} \text{ m}^{-3}$ and $\bar{\gamma} = 0.5$. After 100 s, the targets are changed to be defined by the solution of (16) with $d/dt = 0$ when $\bar{E}_i = 1.45 \times 10^5 \text{ J m}^{-3}$, $\bar{E}_e = 1.88 \times 10^5 \text{ J m}^{-3}$, $\bar{n} = 1.6 \times 10^{20} \text{ m}^{-3}$ and $\bar{\gamma} = 0.5$. In the effector model, the parameters are set to $\eta_{ic} = 0.95$, $\eta_{ec} = 0.9$, $\eta_{nbi_1} = 1$, $\eta_{nbi_2} = 0.85$, $\eta_{Dpel} = 0.97$, $\eta_{DTpel} = 0.92$, $\gamma_{DTpel} = 0.8$ and $\phi_{nbi} = 0.2$. The uncertain parameters in the actuator dynamics θ_u are the same as those presented for scenario B. The initial estimate of the composite uncertainty vector $\hat{\Theta} \triangleq (\hat{\theta}_h^T, \hat{\theta}_u^T, \hat{\theta}_e^T)^T$ is calculated by multiplying the nominal values of each element, in order, with the following numbers: 1.04, 1.09, 0.92, 0.96, 1.07, 0.94, 1.03, 0.94, 1.12, 0.93, 1.05, 0.9, 1.1, 1.13, 0.9, 0.94, 1.1, 0.88, 0.8, 1.05, 1.1, 1.1, 0.87, 0.91 and 0.93.

Figures 6 and 7 show the results of the two simulations for scenario C. For this particular scenario, the adaptive controller with adaptive, dynamic allocation fails to track the reference values when the simpler cost function, J_1 , is used in the allocator's algorithm (see green-dash-dot lines in figure 6). Only when the more complex cost function J_2 (which has barrier functions for the actuator saturation limits) is used, does the burn control scheme successfully track the desired targets (see blue-solid lines in figure 6). Because J_1 does not consider the actuator saturation limits, the allocator's update law (41) commands the ion cyclotron system to provide approximately $P_{ic,d} \approx 22 \text{ MW}$ of heating after 100 s. Because $P_{ic}^{\max} = 20 \text{ MW}$, the burn control scheme with J_1 fails to raise the ion energy to its' target (see figures 6(a) and 7(g)). Without the inclusion of actuator constraints in J_1 , the allocator cannot respond to the saturation of the ion cyclotron power by raising the neutral beam power (to get \bar{E}_i) and lowering the electron cyclotron power (to get \bar{E}_e). The dynamic allocator with J_2 is able to make this response and track the target throughout the simulation run time. Finally, both allocator cost functions sought to minimize the actuation effort (i.e. reduce power and fuel consumption). Therefore, both simulations favored the first neutral beam injector with efficiency factor $\eta_{nbi_1} = 1$ over the second neutral beam injector with efficiency factor $\eta_{nbi_2} = 0.85$ (see figures 7(c) and (g)).

11. Conclusions and future work

Nonlinearity, uncertainty (unknown parameters), actuator allocation, actuator constraints, and actuation lag make burn control more difficult. A Lyapunov-based nonlinear controller was designed to calculate the virtual control efforts that stabilize the system's equilibrium. Adaptive estimation in the controller's algorithm can handle uncertainty in the plasma confinement, particle recycling, impurity sputtering and alpha-particle ion-heating fraction. Particularly for ITER's heating systems, allocation is needed to produce the controller's stabilizing control efforts. Under ideal circumstances where there are no actuator dynamics and the mapping between the virtual control effectors and the actuation efforts (the effector model) is certain, the presented nonadaptive, static allocation algorithm performs competently while taking into consideration the actuator constraints. When uncertain actuator dynamics are included and there exists uncertainty in the effector model parameters such as the neutral beam ion-heating fraction and the tritium concentration of the DT pellets, the performance of the nonadaptive, static allocator will degrade considerably. Due to the modular design of the allocators, the nonadaptive, static allocator can be readily swapped for an adaptive allocation algorithm that consists of dynamic update laws without the need to alter the controller. This burn control scheme with the adaptive allocator is able to overcome the aforementioned challenges when an appropriate cost function was selected for its algorithm.

For future work, the effector model (24) can be expanded to consider DT gas puffing and impurity injection (from gas puffing and pellet injection). Since ITER's neutral beam injectors will heat the plasma by firing highly kinetic deuterium particles into the plasma's core, NBI does supply some fueling to the plasma. Therefore, the deuterium fueling contribution from NBI can be included in the effector model. This would couple the heating actuators to the fueling virtual control efforts in the effector model. In addition, the proposed adaptive, dynamic allocator can be extended to handle time-varying, state-dependent uncertain parameters in the effector model and the actuator dynamics. An example of an uncertain state-dependent parameter is the neutral beam ion-heating fraction (15) which was assumed to be constant in this work. The additional challenge of handling time-varying actuator constraints in burn control applications may also be part of this future work effort to improve the proposed actuator allocator designs. Real-time optimization in the form of receding-horizon optimal control was exploited in the past to tackle time-varying actuator constraints in many plasma control problems, including profile control [32, 33]. Future work may also focus on modeling more specialized actuator dynamics for ITER. This may include pure delays that can be added to the first-order lag processes (25) presented in section 7. These new dynamics would then be considered in the formulation of a new actuator allocator based on a possibly updated effector model. Finally, the burn control schemes presented in this work may be assessed in 1D simulations of ITER before experimental testing (it is anticipated that the burn condition could be 'emulated' to some

extent in present non-burning-plasma devices by using dedicated auxiliary sources). To overcome the issue of limited, noisy plasma diagnostics expected in ITER and future power reactors, the design of state estimators for burn control [34] will need to be further investigated.

Acknowledgments

Work supported by the US Department of Energy, Office of Science, Office of Fusion Energy Sciences, under Award DE-SC0010661.

Disclaimer

This report was prepared as an account of work sponsored by an agency of the US Government. Neither the US Government nor any agency thereof, nor any of their employees, makes any warranty, express or implied, or assumes any legal liability or responsibility for the accuracy, completeness, or usefulness of any information, apparatus, product, or process disclosed, or represents that its use would not infringe privately owned rights. Reference herein to any specific commercial product, process, or service by trade name, trademark, manufacturer, or otherwise, does not necessarily constitute or imply its endorsement, recommendation, or favoring by the US Government or any agency thereof. The views and opinions of authors expressed herein do not necessarily state or reflect those of the US Government or any agency thereof.

Appendix A. Uncertain parameters in plasma model

The lumped uncertain parameters for the plasma model (16) described in section 3 are all positive definite, and they are given by

$$\theta_{h,1} = \frac{1}{\zeta_i H_H}, \quad (45)$$

$$\theta_{h,2} = \frac{1}{\zeta_e H_H}, \quad (46)$$

$$\theta_{h,3} = \phi_\alpha, \quad (47)$$

$$\theta_{h,4} = (1 - \phi_\alpha), \quad (48)$$

$$\theta_{h,5} = \frac{1}{k_\alpha H_H}, \quad (49)$$

$$\theta_{h,6} = \frac{1}{k_D H_H} - \frac{f_{\text{eff}}}{k_D H_H (1 - f_{\text{ref}}(1 - f_{\text{eff}}))} \times \left(f_{\text{ref}} + (1 - \gamma_{\text{PFC}}) \frac{(1 - f_{\text{ref}}(1 - f_{\text{eff}})) R_{\text{eff}}}{1 - R_{\text{eff}}(1 - f_{\text{eff}})} - f_{\text{ref}} \right), \quad (50)$$

$$\theta_{h,7} = \frac{1}{k_T H_H} - \frac{f_{\text{eff}}}{k_T H_H (1 - f_{\text{ref}}(1 - f_{\text{eff}}))} \times \left(f_{\text{ref}} + \gamma_{\text{PFC}} \frac{(1 - f_{\text{ref}}(1 - f_{\text{eff}})) R_{\text{eff}}}{1 - R_{\text{eff}}(1 - f_{\text{eff}})} - f_{\text{ref}} \right), \quad (51)$$

$$\theta_{h,8} = \frac{1}{k_I H_H}, \quad (52)$$

$$\theta_{h,9} = \frac{f_{\text{eff}}(1 - \gamma_{\text{PFC}})}{k_T H_H (1 - f_{\text{ref}}(1 - f_{\text{eff}}))} \times \frac{((1 - f_{\text{ref}}(1 - f_{\text{eff}})) R_{\text{eff}})}{1 - R_{\text{eff}}(1 - f_{\text{eff}}) - f_{\text{ref}}}, \quad (53)$$

$$\theta_{h,10} = \frac{f_{\text{eff}} \gamma_{\text{PFC}}}{k_D H_H (1 - f_{\text{ref}}(1 - f_{\text{eff}}))} \times \frac{(1 - f_{\text{ref}}(1 - f_{\text{eff}})) R_{\text{eff}}}{(1 - R_{\text{eff}}(1 - f_{\text{eff}})) - f_{\text{ref}}}, \quad (54)$$

$$\theta_{h,11} = \frac{f_{\text{Isp}}}{k_I H_H}, \quad (55)$$

$$\theta_{h,12} = f_{\text{Isp}}. \quad (56)$$

Appendix B. Synthesis of burn controller using Lyapunov analysis

The control laws for $P_{\text{aux},i}$, $P_{\text{aux},e}$, S_D and S_T are synthesized by first taking the time derivative of the Lyapunov function V that is given by (18) in section 5:

$$\dot{V} = k_i^2 \tilde{E}_i \dot{\tilde{E}}_i + k_e^2 \tilde{E}_e \dot{\tilde{E}}_e + k_\gamma^2 \tilde{\gamma} \dot{\tilde{\gamma}} + \tilde{n} \dot{\tilde{n}} + \tilde{\theta}_h^T \Gamma_h^{-1} \dot{\tilde{\theta}}_h. \quad (57)$$

The expressions for \tilde{E}_i and \tilde{E}_e are given by (17). With (17), the dynamics of $\tilde{\gamma}$ can be found in a few steps by recalling that $\gamma = n_T/n_H = n_T/(n_D + n_T)$:

$$\dot{\gamma} = \dot{\tilde{\gamma}} = \frac{\dot{n}_T n_H - n_T \dot{n}_H}{n_H^2} = \frac{\dot{n}_T}{n_H} - \gamma \frac{\dot{n}_H}{n_H}, \quad (58)$$

$$\begin{aligned} \dot{n}_H = \dot{\tilde{n}}_H = \dot{\tilde{n}}_T + \dot{\tilde{n}}_D = & -\theta_{h,7} \frac{n_T}{\tau_E^{\text{sc}}} - \theta_{h,6} \frac{n_D}{\tau_E^{\text{sc}}} \\ & + S_D + S_T - 2S_\alpha + \theta_{h,9} \frac{n_T}{\tau_E^{\text{sc}}} + \theta_{h,10} \frac{n_D}{\tau_E^{\text{sc}}}, \\ \dot{\tilde{\gamma}} = \frac{1}{n_H} \left[& -\theta_{h,7} \frac{n_T}{\tau_E^{\text{sc}}} - S_\alpha + S_T + \theta_{h,10} \frac{n_D}{\tau_E^{\text{sc}}} \right. \\ & - \gamma \left(-\theta_{h,7} \frac{n_T}{\tau_E^{\text{sc}}} - \theta_{h,6} \frac{n_D}{\tau_E^{\text{sc}}} - 2S_\alpha + S_D \right. \\ & \left. \left. + S_T + \theta_{h,9} \frac{n_T}{\tau_E^{\text{sc}}} + \theta_{h,10} \frac{n_D}{\tau_E^{\text{sc}}} \right) \right]. \quad (59) \end{aligned}$$

Using (17) and the quasi-neutrality condition that gives $n_e = n_D + n_T + 2n_\alpha + Z_I n_I$, the dynamics of \tilde{n} can be found to be

$$\begin{aligned}
\dot{\tilde{n}} &= \dot{\tilde{n}} = \dot{\tilde{n}}_D + \dot{\tilde{n}}_T + \dot{\tilde{n}}_\alpha + \dot{\tilde{n}}_1 + \dot{\tilde{n}}_e \\
&= 3\dot{\tilde{n}}_\alpha + 2\dot{\tilde{n}}_T + 2\dot{\tilde{n}}_D + (Z_1 + 1)\dot{\tilde{n}}_1, \\
&= -3\theta_{h,5} \frac{n_\alpha}{\tau_E^{\text{sc}}} - 2\theta_{h,7} \frac{n_T}{\tau_E^{\text{sc}}} - 2\theta_{h,6} \frac{n_D}{\tau_E^{\text{sc}}} \\
&\quad - (Z_1 + 1)\theta_{h,8} \frac{n_1}{\tau_E^{\text{sc}}} - S_\alpha + 2S_D + 2S_T \\
&\quad + (Z_1 + 1)S_1 + 2\theta_{h,9} \frac{n_T}{\tau_E^{\text{sc}}} + 2\theta_{h,10} \frac{n_D}{\tau_E^{\text{sc}}} \\
&\quad + (Z_1 + 1)\theta_{h,11} \frac{n}{\tau_E^{\text{sc}}} + (Z_1 + 1)\theta_{h,12}\dot{\tilde{n}}.
\end{aligned} \tag{60}$$

Substitution of the expressions for $\dot{\tilde{E}}_i$, $\dot{\tilde{E}}_e$, $\dot{\tilde{n}}$ and $\dot{\tilde{\gamma}}$ into (57) gives

$$\begin{aligned}
\dot{V} &= k_1^2 \tilde{E}_i \left[P_{\text{aux},i} - \theta_{h,1} \frac{\tilde{E}_i}{\tau_E^{\text{sc}}} - \theta_{h,1} \frac{\tilde{E}_i}{\tau_E^{\text{sc}}} + \theta_{h,3} P_\alpha + P_{\text{ei}} \right] \\
&\quad + k_e^2 \tilde{E}_e \left[P_{\text{aux},e} - \theta_{h,2} \frac{\tilde{E}_e}{\tau_E^{\text{sc}}} - \theta_{h,2} \frac{\tilde{E}_e}{\tau_E^{\text{sc}}} \right. \\
&\quad \left. + \theta_{h,4} P_\alpha - P_{\text{ei}} - P_{\text{br}} + P_{\text{oh}} \right] \\
&\quad + \frac{k_\gamma^2 \tilde{\gamma}}{n_H} \left[-\theta_{h,7} \frac{n_T}{\tau_E^{\text{sc}}} - S_\alpha + S_T + \theta_{h,10} \frac{n_D}{\tau_E^{\text{sc}}} \right. \\
&\quad \left. - \gamma \left(-\theta_{h,7} \frac{n_T}{\tau_E^{\text{sc}}} - \theta_{h,6} \frac{n_D}{\tau_E^{\text{sc}}} - 2S_\alpha + S_D \right. \right. \\
&\quad \left. \left. + S_T + \theta_{h,9} \frac{n_T}{\tau_E^{\text{sc}}} + \theta_{h,10} \frac{n_D}{\tau_E^{\text{sc}}} \right) \right] \\
&\quad + \tilde{n} \left[-3\theta_{h,5} \frac{n_\alpha}{\tau_E^{\text{sc}}} - 2\theta_{h,7} \frac{n_T}{\tau_E^{\text{sc}}} - 2\theta_{h,6} \frac{n_D}{\tau_E^{\text{sc}}} \right. \\
&\quad + 2S_D + 2S_T - S_\alpha - (Z_1 + 1)\theta_{h,8} \frac{n_1}{\tau_E^{\text{sc}}} \\
&\quad + (Z_1 + 1)S_1 + 2\theta_{h,9} \frac{n_T}{\tau_E^{\text{sc}}} + 2\theta_{h,10} \frac{n_D}{\tau_E^{\text{sc}}} \\
&\quad \left. + (Z_1 + 1)\theta_{h,11} \frac{n}{\tau_E^{\text{sc}}} + (Z_1 + 1)\theta_{h,12}\dot{\tilde{n}} \right] + \tilde{\theta}_h^T \Gamma_h^{-1} \dot{\tilde{\theta}}_h.
\end{aligned} \tag{62}$$

By employing the certainty equivalence principle [35] (assume $\hat{\theta}_h = \theta_h$), the four control laws (19)–(22) in section 5 can be formulated from (62). The four control laws (expressions for $P_{\text{aux},i}$, $P_{\text{aux},e}$, S_D and S_T) are chosen to eliminate terms that are not always negative from (62). Because θ_h is not known, the four control laws depend on the estimates of θ_h (denoted $\hat{\theta}_h$), and this will cause many of the terms to depend on $\hat{\theta}_h$ after substituting for the control laws. Substitution of (19)–(22) into (57) gives

$$\begin{aligned}
\dot{V} &= -\frac{k_1^2 \tilde{E}_i^2}{\tau_E^{\text{sc}}} \theta_{h,1} - \frac{k_e^2 \tilde{E}_e^2}{\tau_E^{\text{sc}}} \theta_{h,2} + k_1^2 \tilde{E}_i \frac{\tilde{E}_i}{\tau_E^{\text{sc}}} \tilde{\theta}_{h,1} \\
&\quad + k_e^2 \tilde{E}_e \frac{\tilde{E}_e}{\tau_E^{\text{sc}}} \tilde{\theta}_{h,2} - k_1^2 \tilde{E}_i P_\alpha \tilde{\theta}_{h,3} - k_e^2 \tilde{E}_e P_\alpha \tilde{\theta}_{h,4} \\
&\quad + 3\tilde{n} \frac{n_\alpha}{\tau_E^{\text{sc}}} \tilde{\theta}_{h,5} + \left(2\tilde{n} - \frac{k_\gamma^2 \tilde{\gamma}}{n_H} \gamma \right) \frac{n_D}{\tau_E^{\text{sc}}} \tilde{\theta}_{h,6}
\end{aligned}$$

$$\begin{aligned}
&+ \left(2\tilde{n} - (\gamma - 1) \frac{k_\gamma^2 \tilde{\gamma}}{n_H} \right) \frac{n_T}{\tau_E^{\text{sc}}} \tilde{\theta}_{h,7} \\
&+ \tilde{n}(Z_1 + 1) \frac{n_1}{\tau_E^{\text{sc}}} \tilde{\theta}_{h,8} + \left(\frac{k_\gamma^2 \tilde{\gamma}}{n_H} \gamma - 2\tilde{n} \right) \frac{n_T}{\tau_E^{\text{sc}}} \tilde{\theta}_{h,9} \\
&+ (\gamma - 1) \frac{k_\gamma^2 \tilde{\gamma}}{n_H} \frac{n_D}{\tau_E^{\text{sc}}} \tilde{\theta}_{h,10} \\
&- \tilde{n}(Z_1 + 1) \frac{n}{\tau_E^{\text{sc}}} \tilde{\theta}_{h,11} - (Z_1 + 1)\tilde{n}\dot{\tilde{\theta}}_{h,12} \\
&- K_T \frac{k_\gamma^2 \tilde{\gamma}^2}{n_H} - K_N \tilde{n}^2 + \tilde{\theta}_h^T \Gamma_h^{-1} \dot{\tilde{\theta}}_h.
\end{aligned} \tag{63}$$

If all of the parameters are known ($\tilde{\theta}_h = 0$), the stability condition

$$\dot{V} = -\frac{k_1^2 \tilde{E}_i^2}{\tau_E^{\text{sc}}} \theta_{h,1} - \frac{k_e^2 \tilde{E}_e^2}{\tau_E^{\text{sc}}} \theta_{h,2} - K_T \frac{k_\gamma^2 \tilde{\gamma}^2}{n_H} - K_N \tilde{n}^2 \leq 0, \tag{64}$$

is satisfied ($\tau_E^{\text{sc}}, \theta_{h,1}, \theta_{h,2}, n_H > 0$). Since the estimates of the uncertain parameters are generally inaccurate ($\hat{\theta}_h \neq \theta_h$), the stability condition (64) does not hold with the control laws alone. Therefore, the control laws should be augmented with an adaptive law that estimates θ_h . The adaptive law (23) in section 5 reduces (63) to (64). Therefore, the adaptive law (23) maintains the stability condition (64) when uncertainty exists. It does not guarantee that the estimation errors of the uncertain parameters are driven to zero ($\hat{\theta}_h \rightarrow 0$). The set E is defined by all points of the state space ($\tilde{E}_i, \tilde{E}_e, \tilde{\gamma}, \tilde{n}, \tilde{\theta}_h$) where $\dot{V} = 0$. From (64), it is possible to see that $\dot{V} = 0$ only when $\tilde{E}_i = 0$, $\tilde{E}_e = 0$, $\tilde{\gamma} = 0$ and $\tilde{n} = 0$, regardless of the value of $\tilde{\theta}_h$. Therefore by LaSalle's theorem [5], $\tilde{E}_i, \tilde{E}_e, \tilde{\gamma}$ and \tilde{n} approach zero as $t \rightarrow \infty$.

The stability of \tilde{n}_α can be shown with the Lyapunov function

$$V_\alpha = \frac{\tilde{n}_\alpha^2}{2}. \tag{65}$$

Using (16), its derivative is given by

$$\dot{V}_\alpha = \tilde{n}_\alpha \left(-\theta_{h,5} \frac{n_\alpha}{\tau_E^{\text{sc}}} + S_\alpha \right). \tag{66}$$

With the stabilization of $\tilde{E}_i, \tilde{E}_e, \tilde{\gamma}$ and \tilde{n} , the expression $(-\theta_{h,5} n_\alpha / \tau_E^{\text{sc}} + S_\alpha)$ in (66) increases with decreasing n_α and vice versa. Therefore, the statement

$$\left(-\theta_{h,5} \frac{n_\alpha}{\tau_E^{\text{sc}}} + S_\alpha \right) = -\mu \tilde{n}_\alpha, \tag{67}$$

where μ is a positive continuous function, is valid. The stability of \tilde{n}_α can now be shown with the following condition: $\dot{V}_\alpha = -\mu \tilde{n}_\alpha^2 < 0 \forall \tilde{n}_\alpha \neq 0$ when $\tilde{E}_i = \tilde{E}_e = \tilde{\gamma} = \tilde{n} = 0$.

Finally, the stability of \tilde{n}_1 can be shown using the response model for the impurity density (7). It reduces to $0 = -n_1 + f_1^{\text{sp}} n$ at steady-state (recall that the impurity sputtering is given by $S_1^{\text{sp}} = f_1^{\text{sp}}(n/\tau_1 + \dot{n})$). Clearly, $\tilde{n}_1 = 0$ when $\tilde{n} = 0$. Therefore, bringing the total plasma density (n) to its desired target ($\tilde{n} \rightarrow 0$) is equivalent to stabilizing \tilde{n}_1 .

Appendix C. Synthesis of low-level controller using Lyapunov analysis

All six of the low-level control laws take the same form because the dynamics of each actuator take the form (25). Recalling (25), using the definition of Θ_u (44), taking the time derivative of $V_{\tilde{u},i}$ (42) from section 9 and substituting for $\tilde{u}_i = (u_i - u_{d,i})$ gives

$$\begin{aligned} \dot{V}_{\tilde{u},i} &= \tilde{u}_i \dot{\tilde{u}}_i = \tilde{u}_i (\Theta_{u,i} (u_{\text{cmd},i} - \tilde{u}_i - u_{d,i}) - \dot{u}_{d,i}) \\ &\text{for } i \in \{1, \dots, 6\}. \end{aligned} \quad (68)$$

When $\hat{\Theta}_{u,i} = \Theta_{u,i}$, the stability condition

$$\dot{V}_{\tilde{u},i} = -\tilde{u}_i^2 \hat{\Theta}_{u,i} < 0 \quad \forall \tilde{u}_i \neq 0, \quad (69)$$

is achieved (for $\Theta_{u,i} > 0$) with the low-level actuator control law (43) given in section 9.

ORCID iDs

V. Graber  <https://orcid.org/0000-0003-2058-2258>

References

- [1] Schuster E., Krstic M. and Tynan G. 2002 Burn control in fusion reactors via nonlinear stabilization techniques *Fusion Sci. Technol.* **43** 18–37
- [2] Boyer M.D. and Schuster E. 2014 Nonlinear control and online optimization of the burn condition in ITER via heating, isotopic fueling and impurity injection *Plasma Phys. Control. Fusion* **56** 104004
- [3] Boyer M.D. and Schuster E. 2015 Nonlinear burn condition control in tokamaks using isotopic fuel tailoring *Nucl. Fusion* **55** 083021
- [4] Pajares A. and Schuster E. 2017 Nonlinear burn control using in-vessel coils and isotopic fueling in ITER *Fusion Eng. Des.* **123** 607–11
- [5] Khalil H. 2001 *Nonlinear Systems* 3rd edn (Englewood Cliffs, NJ: Prentice-Hall)
- [6] Wesson J. 1997 *Tokamaks* 2nd edn (Oxford: Clarendon)
- [7] Shimada M. *et al* 2000 Physics design of ITER-FEAT *J. Plasma Fusion Res.* **3** 77–83
- [8] Graber V. and Schuster E. 2019 Nonlinear adaptive burn control of two-temperature tokamak plasmas *58th IEEE Conf. Decision and Control* (Nice, France, 11–13 December) pp 3239–44
- [9] Graber V. and Schuster E. 2020 Nonlinear adaptive burn control and optimal control allocation of over-actuated two-temperature plasmas *American Control Conf.* (Denver, USA, 1–3 July) (<https://doi.org/10.23919/ACC45564.2020.9147885>)
- [10] Combs S.K. *et al* 2012 Overview of recent developments in pellet injection for ITER *Fusion Eng. Des.* **87** 634–40
- [11] Snipes J.A. *et al* 2012 Actuator and diagnostic requirements of the ITER plasma control system *Fusion Eng. Des.* **87** 1900–6
- [12] Johansen T.A. and Fossen T.I. 2013 Control allocation—a survey *Automatica* **49** 1087–103
- [13] Kudláček O. *et al* 2021 Developments on actuator management, plasma state reconstruction, and control on ASDEX Upgrade *Fusion Eng. Des.* **171** 112563
- [14] Pajares A. and Schuster E. 2021 Integrated control and actuator management strategies for internal inductance and normalized beta regulation *Fusion Eng. Des.* **170** 112526
- [15] Pajares A., Schuster E., Welander A., Barr J., Eidielis N., Thome K. and Humphreys D. 2020 Integrated control of individual scalars to regulate profiles and improve mhd stability in tokamaks *28th IAEA Fusion Energy Conf.* (Nice, France, 10–15 May)
- [16] Harkegard O. and Glad S.T. 2005 Resolving actuator redundancy—optimal control vs control allocation *Automatica* **41** 137–44
- [17] Tjonnas J. and Johansen T.A. 2007 Optimizing adaptive control allocation with actuator dynamics *46th IEEE Conf. on Decision and Control* (New Orleans, USA, 12–14 December) pp 3780–5
- [18] Ehrenberg J. 1996 Wall effects on particle recycling in tokamaks *Physical Processes of the Interaction of Fusion Plasmas with Solids* (New York: Academic) p 35
- [19] Bosch H.S. and Hale G.M. 1992 Improved formulas for fusion cross-sections and thermal reactivities *Nucl. Fusion* **32** 611–31
- [20] Gross R. 1984 *Fusion Energy* (New York)
- [21] Doyle E. *et al* 2007 Chapter 2: plasma confinement and transport *Nucl. Fusion* **47** 2175–249
- [22] Shimada M. *et al* 2007 Chapter 1: overview and summary *Nucl. Fusion* **47** S1–S17
- [23] Gallart D., Mantsinen M. and Kazakov Y. 2015 Modelling of ICRF heating in DEMO with special emphasis on bulk ion heating *AIP Conf. Proc.* **1689** 060004
- [24] Hemsworth R.S. *et al* 2017 Overview of the design of the ITER heating neutral beam injectors *New J. Phys.* **19** 025005
- [25] Graber V. and Schuster E. 2021 Assessment of the burning-plasma operational space in ITER by using a control-oriented core-SOL-divertor model *Fusion Eng. Des.* **171** 112516
- [26] Pajares A. and Schuster E. 2019 Robust nonlinear burn control in ITER to handle uncertainties in the fuel-line concentrations *Nucl. Fusion* **59** 096023
- [27] Ravensbergen T., de Vries P.C., Felici F., Blanken T.C., Nouailletas R. and Zabeo L. 2017 Density control in ITER: an iterative learning control and robust control approach *Nucl. Fusion* **58** 016048
- [28] Oppenheimer M.W., Doman D.B. and Bolender M.A. 2006 Control allocation for over-actuated systems *14th Mediterranean Conf. on Control and Automation* (Ancona, Italy, 28–30 June) pp 1–6
- [29] Baylor L.R., Parks P.B., Jernigan T.C., Caughman J.B., Combs S.K., Foust C.R., Houlberg W.A., Maruyama S. and Rasmussen D.A. 2007 Pellet fuelling and control of burning plasmas in ITER *Nucl. Fusion* **47** 443–8
- [30] Boyd S. and Vandenberghe L. 2004 *Convex Optimization* (Cambridge: Cambridge University Press)
- [31] Babenko P.Y., Mironov M.I., Mikhailov V.S. and Zinoviev A.N. 2020 Evaluation of be fluxes into the ITER tokamak plasma due to sputtering of the first wall by D and T atoms leaving the plasma *Plasma Phys. Control. Fusion* **62** 045020
- [32] Ou Y., Xu C., Schuster E., Ferron J.R., Luce T.C., Walker M.L. and Humphreys D.A. 2011 Receding-horizon optimal control of the current profile evolution during the ramp-up phase of a tokamak discharge *Control Eng. Pract.* **19** 22–31
- [33] Maljaars E. *et al* 2017 Profile control simulations and experiments on TCX: a controller test environment and results using a model-based predictive controller *Nucl. Fusion* **57** 126063
- [34] Boyer M.D. and Schuster E. 2014 Nonlinear burn control in tokamak fusion reactors via output feedback *IFAC Proc. Vol.* **47** 3702–7
- [35] Krstić M., Kanellakopoulos I. and Kokotović P.V. 1995 *Nonlinear and Adaptive Control Design* (New York: Wiley)